

Transmission Matrix Inference via Pseudolikelihood Decimation

D. Ancora^{1*}, L. Leuzzi^{1,2},

¹ Institute of Nanotechnology, Consiglio Nazionale delle Ricerche, CNR-NANOTEC - Soft and Living Matter Laboratory, Piazzale A. Moro 2, I-00185, Roma, Italy

² Dipartimento di Fisica, Università di Roma “Sapienza”, Piazzale A. Moro 2, I-00185, Roma, Italy

* daniele.ancora@nanotec.cnr.it

March 1, 2022

Abstract

One of the biggest challenges in the field of biomedical imaging is the comprehension and the exploitation of the photon scattering through disordered media. Many studies have pursued the solution to this puzzle, achieving light-focusing control or reconstructing images in complex media. In the present work, we investigate how statistical inference helps the calculation of the transmission matrix in a complex scrambling environment, enabling its usage like a normal optical element. We convert a linear input-output transmission problem into a statistical formulation based on pseudolikelihood maximization, learning the coupling matrix via random sampling of intensity realizations. Our aim is to uncover insights from the scattering problem, encouraging the development of novel imaging techniques for better medical investigations, borrowing a number of statistical tools from spin-glass theory.

Contents

1	Introduction	2
2	Theoretical Framework	3
2.1	Pseudolikelihood of the I/O model	6
2.1.1	Which partition function?	7
2.2	Pseudolikelihood Derivatives	9
2.3	Measurement Sampling	10
3	Numerical Implementation	10
3.1	Dataset creation and its statistics	11
3.2	\mathcal{L} -maximization with all parameters	12
3.3	Decimation strategy	13
3.3.1	\mathcal{L}_{min} of the fully disconnected model. TBC	14
4	Results	16

4.1	Inferring \mathbb{M} with all the parameters	16
4.1.1	The noise channel as statistical temperature	16
4.1.2	The Transmission matrix	19
4.1.3	Self-Input coupling	19
4.2	Decimation and Information Criterion comparison	19
4.3	The inverse transmission matrix	22
4.4	Pseudo-unity product	25
4.5	Testing image transmission and focusing	25
5	Conclusions and Perspectives	28
	References	32

1 Introduction

Linear problems are largely used in many scientific fields, among which modern topics range from general machine learning aspects [1,2], to spectra deconvolution [3], stock market forecast [4] till the generalization of signal transmission through disordered systems [5]. Among its generality, it is particularly in the latter that our study finds its main motivation. The non-trivial problem of the transmission matrix recovery of an opaque device would enable its usage as an ordinary optical tool, capable to focus or transmit an image through disorder [6,7], turning the scattering into a beneficial feature exploitable to enhance resolution. Turbidity is a random feature of the media depending upon microscopic arrangement of its constituents, and several approaches have been studied to investigate imaging properties in such conditions [8]. The light traveling through a non-uniform environment experiences several changes in its original trajectory due to a random distribution of the refractive index, losing the memory of its initial direction. Although the microscopic process is complicated, the overall effect can be efficiently described with the definition of a transmission matrix [5]. Such matrix describes how an input field is linearly transported into the corresponding output by any arbitrary media and contains the rules on how the medium acts on a given input [5,9,10]. Defining a robust way to measure such matrix is one of the greatest challenges in the field of disordered optics [11] and opens up the usage of new tools for biomedical inspections, such as multimode-fibers [12]. It is not the interest of this paper to describe the benefits for which the community pursues toward this goal, the interested reader could follow more specific modern bibliography [11,13,14]. With our work, instead, we want to offer a novel way to approach the estimation of the transmission matrix via a random sampling statistical approach. The state-of-art for the calculation of the transmission matrix (from now on \mathbb{T}) is the method introduced by Popoff et al. [5], which uses the Hadamard basis as input and reconstruct the \mathbb{T} based on output observations. Although the protocol has proven excellent performance, one would prefer a less strict sampling approach, ideally not relying on any input bases. In fact, the method works only in the forward direction (input to output) and thus gives access only to the direct transmission matrix. Operatively, we need to invert such \mathbb{T} before being able to control the turbid device. Matrix inversion is not a trivial process, especially in the presence

of noise rendering the system very sensitive to perturbation, where it is often preferable other approaches [15]. The need for a procedure that is robust and efficient also for random sampling datasets is the reason why we approach statistics. Breaking the asymmetric approach in [5], further might give access to both the reconstruction of the direct \mathbb{T} and its inverse \mathbb{T}^{-1} with the same technique, opening up novel possibilities to calculate correlations. Our study fits in this context, inferring how we learn the transmission matrix by making use of statistical inference tools.

The model we propose in the following is directly derived from the linear propagation of light in arbitrary media [16] and turns out to be a spin-glass-like model with input/output (I/O) variables, rather than spins. This translation let us use a number of statistical tools to tackle the problem of the \mathbb{T} -parameters inference. In particular, we make use of the pseudolikelihood maximization approach [17, 18] exploiting a decimation strategy [19], to estimate and select the most representative parameters of the I/O model considered. The usage of the pseudolikelihood renders the problem independent, linearly scalable (with the number of parameters) and trivially parallelizable on GPU hardware. Last but not least, our approach could be seen as a thermodynamical alternative to any linear regression problem, thus leaving it generically applicable to any problem involving the solution of linear systems.

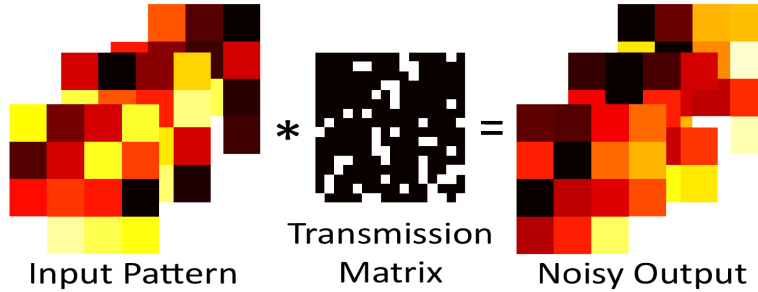


Figure 1: Schematics of the numerical experiment considered. We want to transmit an input signal through a channel characterized by an unknown linear response. The response is fully encoded in the transmission matrix of the system, that gives access to the correct exploitation of the communication channel in both directions.

2 Theoretical Framework

Let us start considering a linear problem with an input-output transmission channel. To keep the analogy with disordered photonics we could see it as an I/O system in which a random medium (such as a multimode fiber) acts as a linear light scrambler: any input vector of intensity distribution $\mathbf{I}^{\text{in}} = \{I_\eta^{\text{in}}\}$, $\eta = 1, \dots, N_I$, is connected to the output pattern $\mathbf{I}^{\text{out}} = \{I_\gamma^{\text{out}}\}$, $\gamma = 1, \dots, N_O$, via an intensity transmission matrix \mathbb{T} by the rule given by:

$$I_\gamma^{\text{out}} = \sum_{\eta=1}^{N_I} T_{\gamma\eta} I_\eta^{\text{in}} + \epsilon_\gamma. \quad (1)$$

Here, we assume for simplicity the number of input modes to be equal to the number of modes recorded at the output $N_O = N_I = N/2$, with $N = N_I + N_O$ and, thus, $\gamma, \eta = 1, \dots, N/2$. We introduced a noise term ϵ_γ in the last term of eq. 1, to be able to include possible statistical perturbations in the measurement, due, e. g., to stochastic temperature changes or to bending or vibrations of the fiber. Such noise term is a random number of zero mean and finite mean square displacement σ_γ . In vector notation, eq. (1) can be compactly written as $\mathbf{I}^{\text{out}} = \mathbb{T}\mathbf{I}^{\text{in}} + \boldsymbol{\epsilon}$. Initially, we will impose $\sigma_\gamma = 0$, $\forall \gamma$.

We point out that eq. (1) describes intensity interactions. It would be exact in the case of imaging incoherent sources (such as fluorescence, phosphorescence, black body radiation, incandescent lamps, etc.). Although similar equations were used for image reconstruction through fiber bundles [20] in interferometric configuration, a rigorous approach would consider complex electromagnetic fields $\mathbf{E}^{\text{out}} = \mathbb{T}_E \mathbf{E}^{\text{in}} + \boldsymbol{\epsilon}$ [21, 22]. In any case, though, we would eventually be bound to learn \mathbb{T} from measures of their intensities $\mathbf{I} = \|\mathbf{E}\|^2$, due to technological limitation, thus an intensity-only model is the only one apt to infer the transmission parameter.

A further implementation considering complex amplitudes as entries [16] would not be qualitatively more complicated than the procedure that we propose here. Our work can be straightforwardly generalized in presence of coherent sources and data available for input and output complex amplitudes (i. e., intensities *and* phases). More complicated, in the case of intensity-only data, is an approach taking into account the phases and our lack of their knowledge: a more strict approach, also much more computationally demanding, would be to average over the unknown phase degrees of freedom with their probability distribution [23]. As we will see, under the assumptions of validity of the present approach, this would be the equilibrium statistical mechanic Boltzmann-Gibbs distribution. In this work, however, we limit ourselves to the model Eq. 1 already able to yield very effective estimates at a rather low computational cost. Thus, in the present representation, \mathbb{T} is a matrix connecting the intensities between the fiber's ends, it is not the exact electromagnetic transmission matrix of the fiber. In the article we refer to it as effective- \mathbb{T} , or simply transmission matrix.

Let us now build the inference model. Satisfying the system equations (1), at zero noise, means requiring that

$$\int \prod_{\gamma=1}^{N/2} dI_\gamma^{\text{out}} \delta \left(I_\gamma^{\text{out}} - \sum_{\eta=1}^{N/2} T_{\gamma\eta} I_\eta^{\text{in}} \right) = 1 \quad (2)$$

for any given entry \mathbf{I}^{in} . The integral (2) can be rewritten expressing each δ -function with a Gaussian in the limit of its standard deviation σ_γ going to zero:

$$\lim_{\sigma \rightarrow 0} \int \prod_{\gamma=1}^{N/2} \frac{dI_\gamma^{\text{out}}}{\sqrt{2\pi\sigma_\gamma^2}} \exp \left\{ -\frac{1}{2\sigma_\gamma^2} \left(I_\gamma^{\text{out}} - \sum_{\eta=1}^{N/2} T_{\gamma\eta} I_\eta^{\text{in}} \right)^2 \right\} = 1 \quad (3)$$

Keeping σ_γ 's finite amounts to introduce Gaussian noise, recovering the noise statistics introduced in eq. (1) for a perturbative term following a Gaussian distribution. For the sake of generality we consider different noise for each output channel γ . If $\sigma_\gamma = \sigma$, $\forall \gamma$ The exponent

in eq. (3) can be expressed as a bilinear cost function:

$$\begin{aligned}
\mathcal{H} &= \sum_{\gamma=1}^{N/2} \left(I_{\gamma}^{\text{out}} - \sum_{\eta=1}^{N/2} T_{\gamma\eta} I_{\eta}^{\text{in}} \right)^2 = \\
&= \sum_{\gamma=1}^{N/2} \left(I_{\gamma}^{\text{out}} \right)^2 - 2 \sum_{\gamma,\eta}^{1,N/2} I_{\gamma}^{\text{out}} T_{\gamma\eta} I_{\eta}^{\text{in}} + \sum_{\gamma,\eta,\eta'}^{1,N/2} T_{\gamma\eta} T_{\gamma\eta'} I_{\eta}^{\text{in}} I_{\eta'}^{\text{in}} \\
&\equiv - \sum_{i,j} I_i J_{ij} I_j = -\mathbf{I}^T \mathbb{J} \mathbf{I}
\end{aligned} \tag{4}$$

where we define the concatenated input-output intensity vector $\mathbf{I} = \{I_{\gamma}^{\text{in}}, I_{\eta}^{\text{out}}\}$ and new indices are defined such that $i, j = \{\gamma, \alpha + N/2\} = \{1, \dots, N\}$. The interaction matrix $\mathbb{J} = \{J_{ij}\}$ has the form of a four-block tensor containing the transmission matrix \mathbb{T} in the out-of-diagonal blocks:

$$\mathbb{J} = \begin{pmatrix} -\mathbb{U} & \mathbb{T}^{\dagger} \\ \mathbb{T} & -\mathbb{I} \end{pmatrix} \tag{5}$$

Here, we can recognize also the input self-coupling matrix $\mathbb{U} = \mathbb{T}^{\dagger} \mathbb{T}$, and the identity matrix \mathbb{I} .

The latter form of eq. (4) is similar to the spin-glass Hamiltonian. In the statistical mechanics formulation \mathcal{H} is the Hamiltonian of the system of which the interaction matrix \mathbb{J} -structured as in eq. 5- is the subject of our inference procedure. Writing $\beta = 1/2\sigma^2$, the stationary probability to have an input-output configuration \mathbf{I} with a certain energy given the set of interaction $\{J_{ij}\}$ is the Boltzmann distribution:

$$P(\mathbf{I}|\mathbb{J}) = \frac{1}{\mathcal{Z}(\mathbb{J}, \mathbf{I})} e^{-\beta \sum_{ij}^{1,N} I_i J_{ij} I_j}. \tag{6}$$

In this context, the normalization Z is the canonical partition function that normalizes the probability distribution:

$$\mathcal{Z}(\mathbb{J}, \mathbf{I}) = \left(\frac{1}{2\pi\sigma^2} \right)^{N/2} \int \prod_{j=1}^N dI_j e^{-\beta \mathcal{H}(\mathbb{J}, \mathbf{I})}. \tag{7}$$

Having defined the probability, it is straightforward to write the log-likelihood \mathcal{L} of the system. The function \mathcal{L} describes how the set of interaction parameters $\{J_{ij}\}$ are likely to describe the observed intensity configuration \mathbf{I} :

$$\mathcal{L}(\mathbf{I}|\mathbb{J}) = \ln [P(\mathbf{I}|\mathbb{J})] \tag{8}$$

Applied to our case, the Maximum Likelihood Estimation (MLE) principle states that the interaction matrix \mathbb{J}_{inf} that maximize the function \mathcal{L} is the one that most likely describe the system interactions:

$$\mathbb{J}_{\text{inf}} = \arg \max \mathcal{L}(\mathbf{I}|\mathbb{J}) \tag{9}$$

We rely on the MLE principle to infer the transmission matrix, introducing a common approximation in the following, due to the fact that \mathcal{L} is very difficult to maximize as the number of degrees of freedom increases.

2.1 Pseudolikelihood of the I/O model

Although there are a few exceptions, maximize \mathcal{L} is challenging. Its computational complexity grows exponentially with the number of parameters, mostly due to the partition function. To have access to analytical solutions linearly scalable with the system size, it is legitimate to introduce the log-pseudolikelihood function \mathcal{L}_i [24] of the i -th element. We follow a common approach tested in spin-glass inference [25, 26], looking at the probability of the i -th element conditional to the realization of the others $\setminus i$:

$$P(I_i | \mathbf{I}_{\setminus i}) = \frac{P(\{I_i, \mathbf{I}_{\setminus i}\})}{P(\mathbf{I}_{\setminus i})}. \quad (10)$$

where $\mathbf{I}_{\setminus i}$ is the set of all intensities but i . Before proceeding with the calculation of the probability $P(I_i | \mathbf{I}_{\setminus i})$, it is useful to explicitly separate the Hamiltonian contributions involving the variable i , \mathcal{H}_i .

Starting from Eq. (3), for a given output pixel variable $\gamma = 1, \dots, N/2$, we can write its contribution to the (temperature rescaled) Hamiltonian as:

$$H_\gamma \equiv \beta_\gamma \mathcal{H}_\gamma(I_\gamma^{\text{out}} | I_{\setminus \gamma}^{\text{out}}, \mathbf{I}^{\text{in}}) = \beta_\gamma \left(I_\gamma^{\text{out}} \right)^2 - 2\beta_\gamma I_\gamma^{\text{out}} \sum_{\eta=1}^{N/2} T_{\gamma\eta} I_\eta^{\text{in}} + \beta_\gamma \sum_{\eta\eta'}^{1, N/2} T_{\eta\gamma}^\dagger T_{\gamma\eta'} I_\eta^{\text{in}} I_{\eta'}^{\text{in}}, \quad (11)$$

where we have explicitly considered a channel dependent “inverse” noise

$$\beta_\gamma \equiv \frac{1}{2\sigma_\gamma^2}. \quad (12)$$

We also define the related partial canonical partition function for the single variable Hamiltonian, given all the other variable values as quenched, as:

$$\mathcal{Z}_\gamma = \int dI_\gamma^{\text{out}} e^{-H_\gamma(I_\gamma^{\text{out}} | I_{\setminus \gamma}^{\text{out}}, \mathbf{I}^{\text{in}})} \quad (13)$$

Analogously, the (noise-rescaled) input variable Hamiltonian contributions relevant to the pseudolikelihood maximization will have the form:

$$H_\eta(I_\eta^{\text{in}} | I_{\setminus \eta}^{\text{in}}, \mathbf{I}^{\text{out}}) \equiv -2I_\eta^{\text{in}} \sum_{\gamma=1}^{N/2} I_\gamma^{\text{out}} \beta_\gamma T_{\gamma\eta} + 2I_\eta^{\text{in}} \sum_{\xi < \eta} V_{\eta\xi} I_\xi^{\text{in}} + \left(I_\eta^{\text{in}} \right)^2 V_{\eta\eta} \quad (14)$$

$$V_{\eta\xi} \equiv \sum_{\gamma} \beta_\gamma T_{\eta\gamma}^\dagger T_{\gamma\xi} \quad (15)$$

$$\mathcal{Z}_\eta = \int dI_\eta^{\text{in}} e^{-H_\eta(I_\eta^{\text{in}} | I_{\setminus \eta}^{\text{in}}, \mathbf{I}^{\text{out}})} \quad (16)$$

We can write the pseudo-likelihood distribution of the generic i -th variable (input or output) given the parameters \mathbb{V} , \mathbb{T} and $\{\beta_\gamma\}$ and the intensities $\mathbf{I}_{\setminus i}$ as:

$$P\left(I_i | \mathbf{I}_{\setminus i}\right) = \frac{e^{-H_i}}{\mathcal{Z}_i}, \quad i = 1, \dots, N \quad (17)$$

and define the related log-pseudolikelihood per each element i as:

$$\mathcal{L}_i = \ln P\left(I_i | \mathbf{I}_{\setminus i}\right) = -H_i - \ln \mathcal{Z}_i \quad (18)$$

In general the maximum likelihood estimation of each single variable pseudo-likelihood function \mathcal{L}_i is carried out searching the parameter's space. In this way the same parameter, say $V_{\eta\xi}$, will be inferred twice, from MLE of \mathcal{L}_η and from MLE of \mathcal{L}_ξ . Since its values are, usually, different, its average value is taken as estimate. Here, we will exploit our knowledge of the symmetry properties of the system in maximizing the sum of all pseudolikelihoods:

$$\mathcal{L} = \sum_{i=1}^N \mathcal{L}_i \quad (19)$$

that we refer to as the total log-pseudolikelihood function. Without loosing specificity, we drop the "log-" prefix and we refer directly to pseudolikelihood (\mathcal{L}) functions.

To put together Eq. (11) and Eq. (14) in Eq. (19) it can be convenient to introduce $N/2 \times N/2$ diagonal matrix β , whose elements are the "inverse temperatures" $\{\beta_\gamma\}$, and to give the following generic expression in terms of $\mathbf{I} = \{\mathbf{I}^{(\text{in})}, \mathbf{I}^{(\text{out})}\}$:

$$H_i = I_i \sum_{j \neq i}^{1,N} M_{ij} I_j + I_i^2 M_{ii} = I_i B_i - I_i^2 A_i, \quad i = 1, \dots, N \quad (20)$$

with

$$\mathbb{M} \equiv \left(\begin{array}{ccc|ccc} \cdot & \cdot & \cdot & -2\mathbb{V} & & \\ & \cdot & -\hat{\mathbb{V}} & \cdot & & 2\mathbb{T}^\dagger \beta \\ -2\mathbb{V} & & \cdot & \cdot & & \\ \hline & & 2\beta \mathbb{T} & & & \\ & & & & \cdot & \cdot \\ & & & & & -\beta \\ & & & & & \cdot \\ & & & & & \cdot \\ & & & & & \cdot \end{array} \right) \quad (21)$$

$$A_i \equiv -M_{ii} \quad , \quad B_i \equiv \sum_{j \neq i}^{1,N} M_{ij} I_j \quad (22)$$

where by $\hat{\mathbb{V}}$ we mean the diagonal part of \mathbb{V} . The partition function is, then, written as:

$$\mathcal{Z}_i = \int dI_i e^{-H_i} \quad (23)$$

By definition the diagonal part of \mathbb{M} is always negative, cf. Eqs. (15) and (21): $A_i = \sum_{j=1}^{N/2} \beta_j T_{ji}^2 > 0$, for $i = 1, \dots, N/2$ and $A_i = \beta_{i-N/2} > 0$, for $i = N/2 + 1, \dots, N$, so that the partition function converges without worrying about the intensity saturation cut-off, that is, the dominion of I_i in integral Eq. (23).

We stress that, since \mathbb{M} is symmetric, only the elements $M_{i \leq j}$ will be inferred, since there are at most $N(N+1)/2$ independent terms. In case of sparse transmission matrices the MLE of the \mathcal{L} is, then, followed by a decimation procedure [19], in which small couplings are recursively set to zero until \mathcal{L} is stable.

2.1.1 Which partition function?

It is obvious that \mathcal{L}_i depends upon the choice of the integration range in the partition function. This choice is bound to the values each I_i can take. First of all, it is possible to analytically

solve the indefinite integral 23, obtaining:

$$\mathcal{Z}_i(I_i) = \sqrt{\frac{\pi}{4A_i}} e^{\frac{B_i^2}{4A_i}} \operatorname{erf}\left(\frac{2A_i I_i - B_i}{\sqrt{4A_i}}\right) \equiv \sqrt{\frac{\pi}{4A_i}} e^{\frac{B_i^2}{4A_i}} \mathcal{F}(I_i). \quad (24)$$

The only term dependent on I_i is the argument of \mathcal{F} , which changes upon different choice of

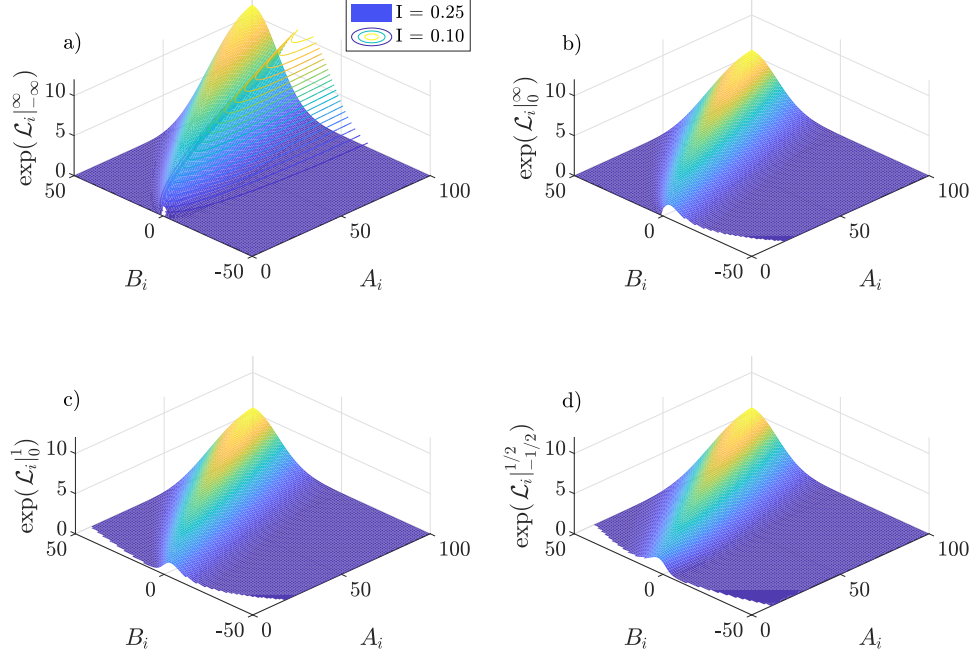


Figure 2: Pseudolikelihood for the i -th intensity elements given all the others. The function is plotted against the parameters A_i and B_i , using $I_i = 0.25$ as a reference value for the intensity. In the first plot we draw the contours lines for a different case $I = 0.10$. Although the plots differ in terms of absolute values, it is possible to notice how the maximum follow the same direction in all the cases.

the integral limits $[I_{min}, I_{max}]$ as, for instance:

$$\mathcal{F}_i = \begin{cases} 2 & \text{for } \mathcal{F}_i|_{-\infty}^{\infty} \\ 1 + \operatorname{erf}\left(\frac{B_i}{\sqrt{4A_i}}\right) & \text{for } \mathcal{F}_i|_0^{\infty} \\ \operatorname{erf}\left(\frac{2A_i - B_i}{\sqrt{4A_i}}\right) + \operatorname{erf}\left(\frac{B_i}{\sqrt{4A_i}}\right) & \text{for } \mathcal{F}_i|_0^1 \\ \operatorname{erf}\left(\frac{2A_i - B_i}{\sqrt{4A_i}}\right) + \operatorname{erf}\left(\frac{2A_i + B_i}{\sqrt{4A_i}}\right) & \text{for } \mathcal{F}_i|_{-1}^1 \end{cases} \quad (25)$$

We stress that the intensities of the pixels are defined as positive quantities. As we will see in the following, though, letting them run along negative values, as well, does not alter the inference quality and allows for a simplified computation. The correct selection of the integral limits should take into account all the possible intensities allowed in the system. In

this framework, the \mathcal{L}_i can be explicitly written as:

$$\mathcal{L}_i = I_i B_i - I_i^2 A_i - \frac{1}{2} \ln \left(\frac{\pi}{4A_i} \right) - \frac{B_i^2}{4A_i} - \ln \mathcal{F}_i \Big|_{I_{min}}^{I_{max}}. \quad (26)$$

To have a graphical view on the various functions introduced in eq. (26), we plot the generic pseudolikelihood as a function of the parameters $\exp(\mathcal{L}_i) = P(A_i, B_i | I_i)$ at given I_i , for different choices of the integration extremes in Fig. 2. We can qualitatively appreciate how the maxima of the functions follow the same direction along the plane (A_i, B_i) . As I_i varies the maximum of $P(A_i, B_i | I_i)$ varies¹. We consider four cases though the simplest choice of $\mathcal{F}_i|_{-\infty}^{\infty} = 2$ turns out to be operatively the most efficient for all the intensities tested.

2.2 Pseudolikelihood Derivatives

The formulation of the pseudolikelihood (26) defines a concave function that admits (under low enough noise) a unique maximum. To ease the maximization process is, thus, useful to calculate its first derivatives. Let us first compute the derivatives of the parameters A'_i and B'_i , defined in eq. (22), to simplify the notation:

$$A'_i = \frac{\partial A_i}{\partial M_{nm}} = -\delta_{in} \quad B'_i = \frac{\partial B_i}{\partial M_{nm}} = \delta_{in} \delta_{jm} I_j. \quad (27)$$

It is now possible to calculate the derivatives of \mathcal{L}_i with respect to the parameters of the interaction matrix \mathbb{M} :

$$\frac{\partial \mathcal{L}_i}{\partial M_{nm}} = I_i B'_i - \frac{1}{[\mathcal{F}_i]} \frac{\partial \mathcal{F}_i}{\partial M_{nm}}, \quad (28)$$

$$\frac{\partial \mathcal{L}_i}{\partial M_{nn}} = -I_i^2 A'_i + \frac{A'_i}{2A_i} - \frac{1}{[\mathcal{F}_i]} \frac{\partial \mathcal{F}_i}{\partial M_{nn}}. \quad (29)$$

Of course, the derivatives of \mathcal{F}_i depend upon the choice of the integration limits thus, for the cases analyzed in 2.1.1, we have that the out of diagonal terms of \mathbb{M} can be expressed as:

$$\frac{\partial \mathcal{F}_i}{\partial M_{nm}} = B'_i \left(\frac{e^{-\frac{B_i^2}{4A_i}}}{\sqrt{\pi A_i}} \right) \begin{cases} 0 & \text{for } \mathcal{F}_i|_{-\infty}^{\infty} \\ 1 & \text{for } \mathcal{F}_i|_0^{\infty} \\ 1 - e^{-A_i+B_i} & \text{for } \mathcal{F}_i|_0^1 \\ e^{-A_i-B_i} - e^{-A_i+B_i} & \text{for } \mathcal{F}_i|_{-1}^1 \end{cases}, \quad \forall n \neq m \quad (30)$$

and the diagonal part gives:

$$\frac{\partial \mathcal{F}_i}{\partial M_{nn}} = -\frac{A'_i}{2A_i} \left(\frac{e^{-\frac{B_i^2}{4A_i}}}{\sqrt{\pi A_i}} \right) \begin{cases} 0 & \text{for } \mathcal{F}_i|_{-\infty}^{\infty} \\ B_i & \text{for } \mathcal{F}_i|_0^{\infty} \\ B_i - e^{-A_i+B_i} (B_i + 2A_i) & \text{for } \mathcal{F}_i|_0^1 \\ e^{-A_i-B_i} (B_i - 2A_i) - e^{-A_i+B_i} (B_i + 2A_i) & \text{for } \mathcal{F}_i|_{-1}^1 \end{cases}. \quad (31)$$

These derivatives are a sufficient requirement to use quasi-Newtonian methods for finding the maximum of a function, without explicitly calculating the Hessian. However, second derivatives can be explicitly calculated, even if the algorithm should pose dedicated care to avoid out-of-memory issues.

¹We do not have a unique maximum, since it will be given by the choice of the $\{J_{ij}\}$ rather than the two parameters of eq. (22)

2.3 Measurement Sampling

Having set a statistical framework, we have to consider the quantities introduced above as averaged over M measurements:

$$\mathcal{L} = \frac{1}{M} \sum_{i=1}^N \sum_{\mu=1}^M \mathcal{L}_{i,\mu} \quad (32)$$

This depends on the $N \times N$ M_{ij} coupling parameters. However, for the symmetry properties of Eq. (20), only $N(N+1)/2$ of them are independent. We maximize \mathcal{L} only with respect to those, forming the lower triangle M_{ij} , $i \leq j$, of matrix (21), including the diagonal. The $N(N+1)/2$ derivatives are, then,

$$\frac{\partial \mathcal{L}}{\partial M_{nm}} = \frac{1}{M} \sum_{i=1}^N \sum_{\mu=1}^M \frac{\partial \mathcal{L}_{i,\mu}}{\partial M_{nm}} \quad (33)$$

where M is the number of coupled I/O observations of a system with a fixed \mathbb{T} . The sampling rate of a given system will impact on the inference procedure: a larger statistical sampling will correspond to a more accurate learning process, i. e., to a better estimate of the model parameters. Thus, we define the sampling rate $\xi(M, K)$ as:

$$\xi(M, K) = \frac{M}{K} \quad (34)$$

where ξ depends on the number of parameters K to be inferred in the model and on the parameters. Three situations can occur in this case, depending on the sampling rate achieved:

- $\xi < 1$, undersampling regime: the number of measurements is lower than the number of parameters, worst inference scenario.
- $\xi \gtrsim 1$, sufficient sampling: M approximately matches K , thus the sampling rate is appropriate for a stable learning procedure.
- $\xi \gg 1$, oversampling regime: best case scenario, in which the number of measurements is high enough to reasonably rule out pre-asymptotic finite measurement effects in the convergence of the pseudolikelihood to the actual likelihood function.

Ideally, we would like to be able to correctly infer the parameters in all the possible sampling rates, in particular in the undersampled regime. In the following, we will try to analyze the behaviour of our learning framework under different measurement scenarios.

3 Numerical Implementation

The algorithm is written in MATLAB, making use of the unconstrained minimization routine `minFunc` [27] enjoying the L-BFGS algorithm, which uses a low-rank Hessian approximation. This lets the system accept a higher number of variables, keeping the lowest memory usage. Of course we are not bound to use L-BFGS algorithms for the optimization, but we found it a good compromise between accuracy, speed and memory requirement. We also have tested the use of constrained optimization since we have full control on the parameter range in the system. However, we decided to report unconstrained results to be more general and to assess the robustness of the method.

3.1 Dataset creation and its statistics

To test the inference model, we created numerically a set of intensity measurements, to simulate a laboratory experiment. First of all, any real camera measurement returns a positive value for the intensity, limited in magnitude by the camera sensitivity: values above the camera maximal sensitivity I_{\max} will saturate and below the minimal sensitivity I_{\min} will not be recorded. For the sake of generality, we rescale these values and we assume that our simulated camera works in the range $I_i \in [0, 1]$ for both the input and the output. For the input, we choose to generate M squared patterns of pixels having size w . Each of these contains $N_I = N_O = N/2 = w^2$ random values normally distributed, accordingly to a truncated gaussian probability distribution with $\sigma^{\text{in}} = 0.1$, $\forall \gamma$ and $\mu = 0.5$. We point out that σ^{in} is not related to the noise, but defines the distribution of intensity values sampled in the input. These patterns are transported into the corresponding outputs via the \mathbb{T} matrix, that must preserve the positiveness and the intensity range.

In order to build our \mathbb{T} we first decide that a fraction s of all possible entries will be active (non-zero), i. e., $s = S_{\text{active}}/w^4$. Given the sparsity, we randomly activate S_{active} couplings in a temporary (binary) \mathbb{T}' -matrix, setting their value to 1. We want also the output to be in the same $[0, 1]$ range, thus, we need to normalize the \mathbb{T}' row wise, so that the matrix eventually be a stochastic matrix:

$$T_{\gamma\alpha} = \frac{T'_{\gamma\alpha}}{\sum_{\alpha} T'_{\gamma\alpha}} \quad , \quad \sum_{\alpha=1}^{N_O} T_{\gamma\alpha} = 1$$

With this choice, in every experiment performed we are guaranteed to have also the output in the same intensity range of the input, as it is the case for CCD camera acquisitions. In general, we found that the histogram of the intensities in the output followed a narrower Gaussian distribution, as it can be seen in Fig. 3. Depending on which integral (25) is chosen

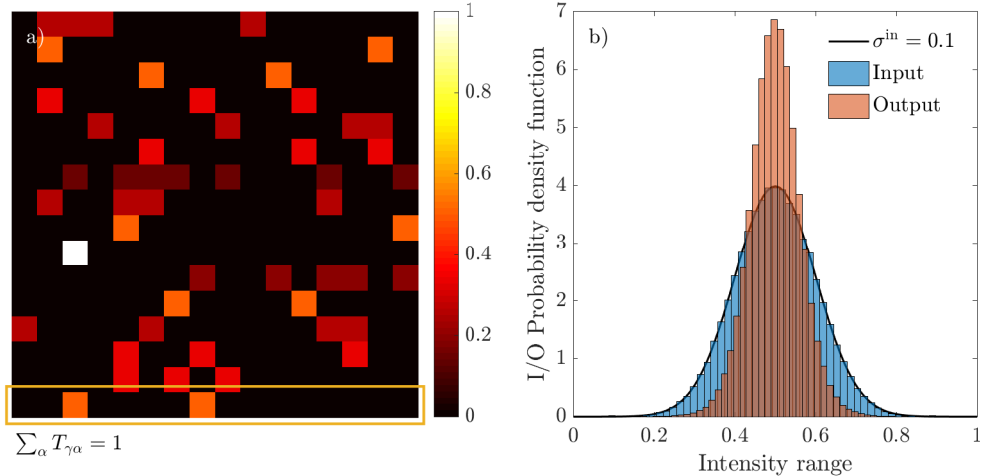


Figure 3: On the left, an example of a transmission matrix for a 4x4 input-output system. On the right the probability distribution chosen for all the pixel in the input (blue histogram) and the corresponding distribution after passing through the transmission channel (orange histogram). Both have gaussian statistics with mean value centered at 0.5.

for the inference, when the region of integration is taken symmetric around zero (explicitly, when we use $\mathcal{F}_i|_{-\infty}^{\infty}$ or $\mathcal{F}_i|_{-1/2}^{1/2}$), it is convenient to translate the intensities in each channel by their mean $I_i - \mu_i$. The reason for this will be discussed in section 3.3.1 and in the Results.

Accordingly to (2), we will study the inference method under noisy measurements. We add a perturbative noise term to the output, leaving the input unaltered. The noise is a Gaussian random number with zero mean and variance σ . To probe different noise regimes we repeated our analysis changing $\sigma \in [0, 0.5]$, in steps of 0.02, including possible strong saturation effects of the data. Per each σ , we will run an optimization and consequently a full decimation of the parameters, studying the best model selection via the usage of several information criteria. The effect introduced by the noise perturbation is represented in Fig.4; where it is clear that when the noise grows up to 20%, the channel is so perturbed that saturation effects become relevant.

3.2 \mathcal{L} -maximization with all parameters

We decided to start the optimization process using weak prior information. Recalling the tensor form of the \mathbb{M} , we initialize each block with the following criteria:

1. \mathbb{I} block, we start with a diagonal unity matrix;
2. \mathbb{T} blocks, we set all the parameters to $1/w^2$;
3. \mathbb{V} block, we calculate it as $\mathbb{T}^\dagger \boldsymbol{\beta} \mathbb{T}$ using the previously initialized matrix, with $\beta_\gamma = \beta = 1/2/\sigma, \forall \gamma$.

We call the initial coupling matrix as $\mathbb{M}^{(0)}$ and we run the minimization routine, obtaining the estimated couplings $\{M_{ij}\}$. We point out, that any initialization scheme should lead to the

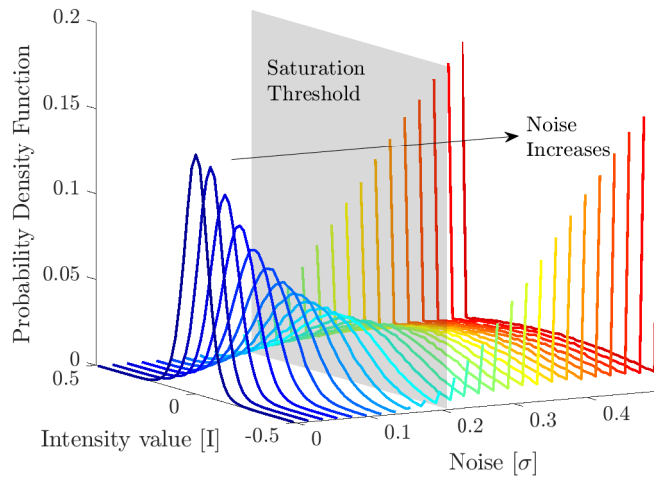


Figure 4: Statistics of the output intensities after perturbing the channel with noise at increasing variance. The jet colorbar on the right is synchronized with the noise variance. The effect is that the original distribution starts to widen and saturation effects appear at around $\sigma = 0.2$. The two wings represent an increased saturation effect due to very strong noise.

same optimal convergence for the parameters, but with the described choice we avoid potential wrong starting directions in the optimization process, leading to no or slow convergence. In particular, for the \mathbb{I} region we immediately decimate the out-of-diagonal elements, that never take part in the optimization. The resulting optimized interaction matrix is referred to as \mathbb{M}_{inf} .

3.3 Decimation strategy

After the initial \mathcal{L} -maximization, we proceed decimating the region where the smallest couplings are inferred. Our assumption is that the transmission matrix has a certain degree of sparsity, which we want to recover during the learning procedure in order to avoid overfitting. We proceed iteratively, sorting the values of the inferred \mathbb{T} and discarding a fraction, equal to $1/128$, of the smallest elements. Then, we repeat again the optimization starting with the previously inferred matrix. Ideally, the absolute value of the maximum \mathcal{L} should follow a constant behaviour while decimating irrelevant couplings, while a decrease is expected when discarding relevant parameters. The decimation strategy is directly applied on the \mathbb{T} -region via the definition of a binary parameter mask \mathbb{T}^{bin} , which is $T_{ij}^{\text{bin}} = 1$ when the coupling is active and 0 otherwise. The decimation is transported into the \mathbb{V} -region by calculating another mask $\mathbb{V}^{\text{bin}} = (\mathbb{T}^{\text{bin}})^\dagger \beta \mathbb{T}^{\text{bin}}$. We restrict the decimation procedure only in the out-of-diagonal part of \mathbb{M} , thus leaving the diagonal parameters $\{M_{ii}\}$ acting as regularizers at advanced stages of decimation, in order to avoid divergence of the partition function. Per each decimation step, we call K the total number of active parameters in \mathbb{M} .

Decimation was introduced in [19] to estimate couplings in an Ising model along with a stopping criterion, which allows us to estimate an appropriate number of parameters without proceeding further with the decimation. In this work, we decide to compare several information criteria (IC) that can be used to decide where to stop the decimation when a good \mathbb{M} estimate is achieved.

- **Tilted-Pseudolikelihood Information Criterion (TIC):** Following the procedure introduced by Decelle and Ricci-Tersenghi in [19] we define the tilted- \mathcal{L} information criterion (we call it TIC for nomenclature consistency with the others) as

$$\text{TIC} = \mathcal{L} - k\mathcal{L}_{\text{max}} - (1 - k)\mathcal{L}_{\text{min}} \quad (35)$$

where $k = K/C_{\text{total}}$ is the fraction of the active and $(1 - k)$ the fraction of the decimated couplings. \mathcal{L}_{max} is the value achieved maximizing the fully connected model while \mathcal{L}_{min} is the pseudolikelihood of the non-interacting model. Ideally, we want to stop the decimation when $k^* = s$, the true fraction of non-zero elements in \mathbb{T} , as defined in Sec. 3.1. By definition, k^{TIC} is the value at which TIC is maximized, and \mathbb{M}^{TIC} is the optimized decimated interaction matrix.

- **Akaike information Criterion (AIC):** The first criterion to estimate the optimal parameter number in a given model was introduced by Akaike's work [28], as:

$$\text{AIC} = 2K - 2M(\mathcal{L}) \quad (36)$$

The value K^{AIC} at which the AIC is minimized correspond to the model matrix \mathbb{M}^{AIC} that minimizes the information loss, thus, at the best parameter number representing the system.

- **Corrected AIC (AICc):** When the sampling M is small (though larger than K), there is a higher chance that AIC will overfit, selecting models with a higher number of parameters. To take into account this, a modified version of the AIC, namely AICc, was introduced [29]:

$$\text{AICc} = \text{AIC} + \frac{2K(K+1)}{M-K-1} \quad (37)$$

The above formulation takes into account the sampling number into a penalty factor, that loses importance when $M \rightarrow \infty$ converging to AIC value. The value K^{AICc} at which the AICc is minimized corresponds to a second-order estimate of the optimal model. \mathbb{M}^{AICc} is the corresponding decimated matrix.

- **Bayesian Information Criterion (BIC):** Firstly introduced by Schwarz in [30], it can be written as a function of the estimable parameters K and the number of sampling M as:

$$\text{BIC} = K \log(M) - 2M\mathcal{L}. \quad (38)$$

The number of parameters K^{BIC} at which BIC is minimized is the best inference point accordingly to the Bayesian information criterion. Here, the interaction matrix selected is called \mathbb{M}^{BIC} . This method resulted efficient in the activation method [31] for the inference of Ising couplings starting from empty matrices.

The information criteria introduced will help us to estimate the best model fitting the data, giving an indication on the sparsity and the corresponding number of parameters needed to correctly describe it.

3.3.1 \mathcal{L}_{\min} of the fully disconnected model. TBC

Accordingly with the decimation strategy proposed in 3.3, when the model is completely decimated only the values on the diagonal of the interaction matrix $\{M_{ii}\}$ are active. This implies that, for each i -th likelihood \mathcal{L}_i , the parameter $B_i = 0$ vanishes. In practice, we are left with:

$$\mathcal{L}_i \xrightarrow[\text{decimation}]{B_i \rightarrow 0} \ln \left(\frac{e^{M_{ii}I_i^2}}{\int dI_i e^{M_{ii}I_i^2}} \right) = \ln \left(\frac{e^{-A_i I_i^2}}{\int dI_i e^{-A_i I_i^2}} \right) \quad (39)$$

The argument of the logarithm is a Gaussian distribution of variance $2/A_i$ with, cf. Eqs. (12), (15),

$$-M_{ii} = A_i = \begin{cases} \frac{1}{2\sigma_{i-N/2}^2} & \text{if } i = N/2 + 1, \dots, N, \quad \text{output} \\ \sum_{\gamma=1}^{N/2} \frac{1}{2\sigma_{\gamma}^2} T_{\gamma i}^2 & \text{if } i = 1, \dots, N/2, \quad \text{input} . \end{cases} \quad (40)$$

When the model is fully decimated, maximizing each \mathcal{L}_i corresponds to fit a Gaussian probability distribution on the distribution of the intensities per channel i . The main limitation is that the decimated model fits a Gaussian distribution fluctuating around a null value. For this reason, a theoretical calculation of the \mathcal{L}_{\min} is possible only if we shift $\mathbf{I} - \boldsymbol{\mu}$, where $\boldsymbol{\mu} = \{\mu_i\}$ is the vector mean value calculated on the M samplings. For the case described in section 3.1 we have that $\mu_i = 0.5 \forall i$, thus it makes sense to shift all the intensities by this value. Let us recall, that in this case we need to use either $\mathcal{L}_i|_{-\infty}^{+\infty}$ or $\mathcal{L}_i|_{-1/2}^{+1/2}$, to accept

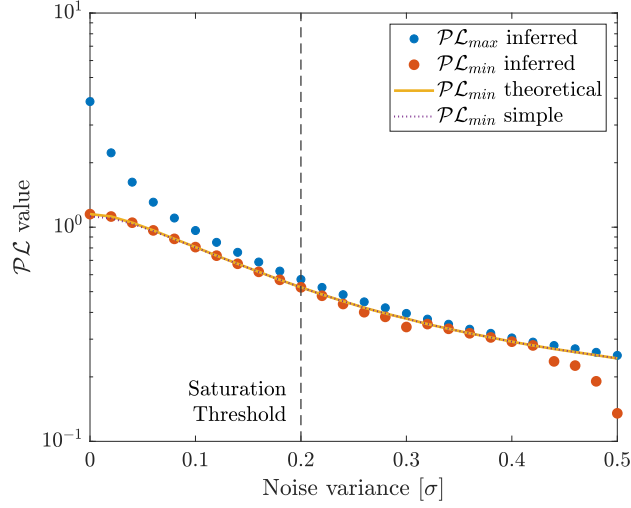


Figure 5: Pseudolikelihood boundaries as a function of the noise plotted in a log-scale. The blue values are the \mathcal{L} minimized with all the parameters, that progressively decimate to the final orange values. The continuous yellow and dashed violet line represents the values expected from the theory, respectively from equations (42) and (43).

negative values of the integration variables. This shift will not change the definition of \mathbb{T} . Now we can calculate the minimum value that \mathcal{L} can reach as:

$$\begin{aligned} \mathcal{L}_{min} \Big|_{-1/2}^{1/2} &= - \sum_{i=1}^N \left[\frac{I_i^2}{2\sigma_i^2} + \ln \left(\frac{\pi\sigma_i^2}{2} \right) + \ln \mathcal{F}_i \Big|_{-1/2}^{+1/2} \right] \\ &= - \frac{1}{2} \sum_{i=1}^N \frac{I_i^2}{\sigma_i^2} - N \ln \frac{\pi}{2} - 2 \sum_{i=1}^N \ln \sigma_i - \sum_{i=1}^N \ln \left[2 \operatorname{erf} \left(\frac{1}{2\sqrt{2}\sigma_i} \right) \right] \end{aligned} \quad (41)$$

or

$$\mathcal{L}_{min} \Big|_{-\infty}^{\infty} = - \frac{1}{2} \sum_{i=1}^N \frac{I_i^2}{\sigma_i^2} - \frac{N}{2} \ln 2\pi - \sum_{i=1}^N \ln \sigma_i. \quad (42)$$

In the scenario in which there are a variance characterizing the input σ_I and one characterizing the output σ_O equiparted between $N/2$ inputs and $N/2$ outputs, the formula above reduces to:

$$\mathcal{L}_{min} = - \frac{1}{2} \left(\frac{1}{\sigma_I^2} \sum_{i=1}^{N/2} I_i^2 + \frac{1}{\sigma_O^2} \sum_{i=N/2+1}^N I_i^2 \right) - \frac{N}{2} \ln (2\pi\sigma_I\sigma_O). \quad (43)$$

For example in the case of 4x4 of Fig. 3, we have $\sigma_I = \sigma^{\text{in}}$ and $\sigma_O = 0.05$. In the following, we will consider the results obtained by a uniform shift of the intensities $\mathbf{I} - 0.5$, thanks to the statistical distribution properties of both input and output (Fig. 3). If we consider this specific case, it is possible to calculate the TIC theoretically for the empty model. In Fig.

5 we plot the numerically optimized minimum and maximum value for the \mathcal{L} , against the theoretical results. The plot clearly tells that the eq. 42-43 predicts the lower boundary for the pseudolikelihood.

4 Results

In the previous chapters, we have extensively described the learning framework proposed for an I/O spin-glass model. In the following we present the results found under different operative conditions, in order to define standard modus operandi. We will always keep an eye on theory, to be able to interpret the results. In order to ease the graphical visualization of the results, we focus on the problem of 4x4 I/O matrix. Such results will be directly extendible to any I/O size, taking into account the possible presence of undersampling problematics that we will examine extensively.

4.1 Inferring \mathbb{M} with all the parameters

To begin, let us focus on the algorithm convergence. We keep all the parameters free to adjust themselves into a form that maximizes the pseudolikelihood without decimation. Here, we explicitly consider the inference results of a 4x4 I/O system, implying a \mathbb{M} matrix of 32x32 parameters. Similar results were found with every size considered, but for the sake of a clear visualization we initially present the results of the smallest system. We consider the minimization with weak noise $\sigma = 0.02$ and a positive \mathbb{T} matrix with $s = 0.2$ sparsity. After maximizing the pseudolikelihood with respect to $M_{i \leq j}$, we obtain the result shown in Fig. 6.

Let us call the inferred matrix \mathbb{M}^{inf} . It is quite clear that the matrix converged into the expected tensorial form given by (21): the green area is the negative part of the matrix, while in red it is represented the positive. We label three parts in the matrix, as shown in the figure:

- Part 1) - The self-output coupling matrix converges into a diagonal form, $-\beta$, whose elements are $\{\beta_{i-N/2}\} = (\beta_1, \beta_2, \dots, \beta_{N/2})$, for $i = N/2 + 1, \dots, N$.
- Part 2) - The input-output coupling matrix closely follows the transmission matrix $2\beta\mathbb{T}$ used for the dataset creation.
- Part 3) - The self-input coupling matrix reported is $-\mathbb{V}$, with, cf. Eq. (15),

$$\begin{aligned} -V_{\eta\xi} &= -\sum_{\alpha=1}^{N/2} T_{\eta\alpha}^\dagger \beta_\alpha T_{\alpha\xi} & \forall \eta, \xi = 1, \dots, N/2, \quad i \leq j, \\ -\mathbb{V} &= -\mathbb{T}^\dagger \beta \mathbb{T} \end{aligned} \quad (44)$$

To better understand how the noise propagates within this matrix, it is convenient to separate the formal analysis per each of the parts labelled in the interaction matrix \mathbb{M} , separating out the noise mask β from matrix (21).

4.1.1 The noise channel as statistical temperature

First of all, it is important to notice that the diagonal term (Part 1 of \mathbb{M}^{inf}) gives us an estimation of the noise per each channel of the system. According to the tensorial form (21),

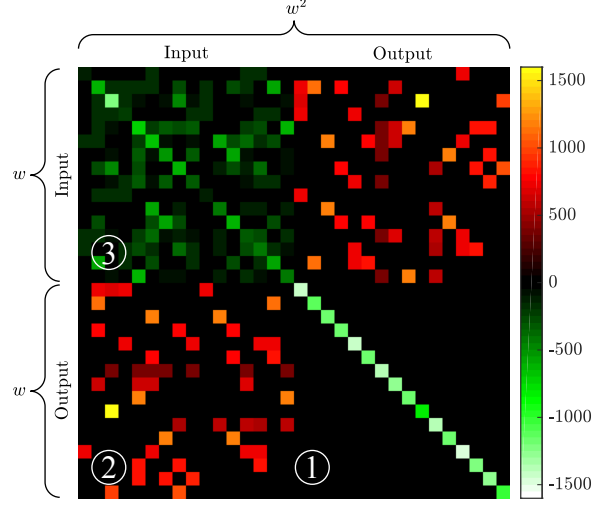


Figure 6: Schematics of the initial inference results: the matrix \mathbb{M} obtained after the \mathcal{L} maximization on independent active parameters. The black regions are the values close to zero, while with green and red we can distinguish between three (respectively negative and positive) different matrix subregions.

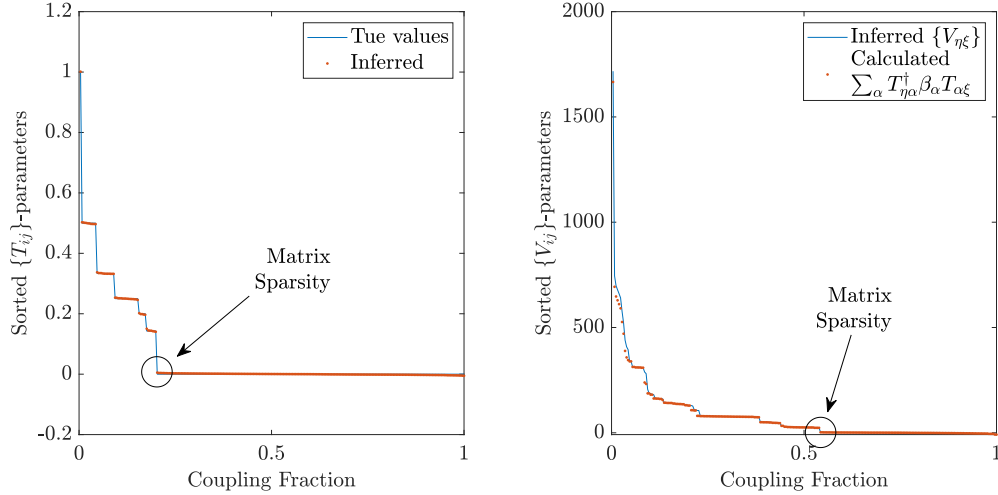


Figure 7: Part a), in orange the sorted values of \mathbb{T}_{inf} against the true values \mathbb{T} (blue line). Part b), sorted values of \mathbb{V}_{inf} against the \mathbb{V} . The plots of parts a-b) are obtained scaling the values in the matrix of part a) with the rules given in sections 4.1.1, 4.1.2 and 4.1.3.

in the diagonal part we have that $M_{ii} = \beta_i$ for $i > N/2$, thus the diagonal elements of \mathbb{M}^{inf} explicitly recovers the noise $\beta_{\gamma=i-N/2}$ per each I/O channel as in eq. (20). It is interesting to see how the perturbative noise statistics can be recovered by looking directly at the diagonal part. We studied a range of noise σ , that we can relate to the factor β_γ for each output channel γ , via: $\beta_\gamma = 1/2/\sigma_\gamma^2$, $\gamma = 1, \dots, N/2$, i. e., in matrix notation,

$$\beta = (2\sigma^2)^{-1} \quad (45)$$

where the diagonal matrix σ is introduced in Eq. (1).

Thus, giving a thermodynamical interpretation, the average temperature of the measurement is:

$$\theta \equiv \frac{2}{N} \sum_{\gamma=1}^{N/2} \frac{1}{\beta_{\gamma}} \quad (46)$$

where, theoretically, the temperature can be expressed in terms of the variance of the noise introduced in Eqs. (3) or (12), $\theta_{th} = 2\sigma^2$. In Fig. 8, we plot the average temperatures, estimated from the inference of the full model for the systems studied, as a function of the noise inserted in the dataset. We can appreciate a pretty good agreement with the theoretical expectation, that is the system temperature scales quadratically with the inserted noise. After a certain point around $\sigma = 0.20$, the estimation departs from the parabolic trend. This effect is due to the effective statistics of the output intensity values in Fig. 4, where an important saturation effect emerges when the noise is high compared to the intensity range accepted by the system.

We can conclude that the diagonal matrix of part 1) is effectively giving an estimation for the noise experienced within each transmission channel. This can be visualized in part b) plot of Fig. 8, where per each channel we calculate the inserted noise standard deviation σ_i^C and we divide it for the estimated one σ_i , as a function of the variance of the noise ϵ introduced in Eq. (1). It is possible to notice that this ratio stays around 1 (the gray plane), indicating that we are effectively estimating the channel noise up to a perturbation of 20%. Beyond this value, the noise estimation starts to depart from the real one due to saturation effects.

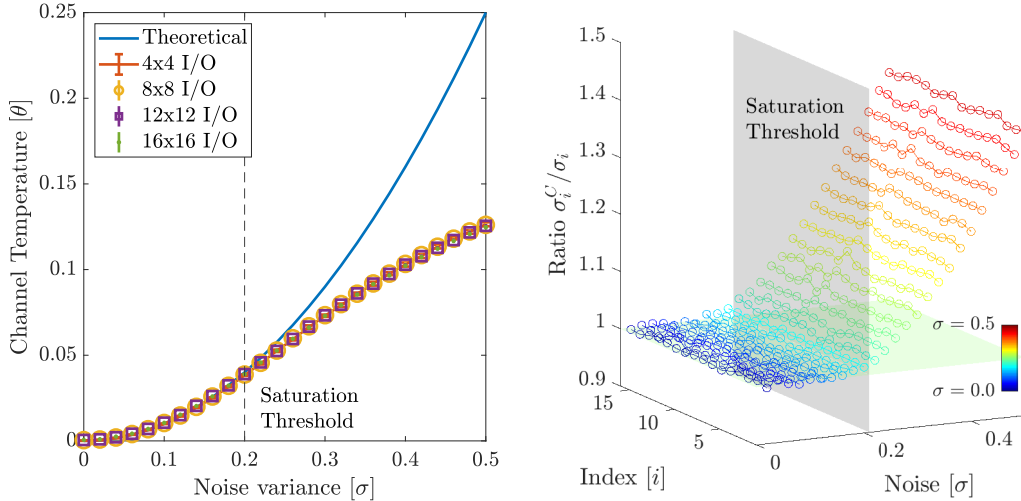


Figure 8: Part a), plot of the mean temperature θ obtained for the four systems tested. The theoretical value (blue dashed line) is calculated with $\theta_{th} = 2\sigma^2$. Part b), plot of the ratio between the calculated variance of the dataset per each line σ_i^C normalized by the σ_i obtained in the diagonal part of matrix \mathbb{M} . The gray plane represents the expected ratio when both the estimation and the effective noise are scaling like the noise inserted in the system σ .

4.1.2 The Transmission matrix

Understanding the diagonal matrix in block (1) gives us the possibility to calculate exactly the transmission matrix elements \mathbb{T}^{inf} from the inferred \mathbb{M}^{inf} block (2): we divide row wise M_{ij}^{inf} for $i \in [1, N/2]$ and $j \in [N/2 + 1, N]$ by the elements β_i , so that the estimation of the system transmission matrix is given by

$$T_{i,j-N/2}^{\text{inf}} = \frac{M_{ij}^{\text{inf}}}{2\beta_i}. \quad (47)$$

Part a) of Fig. 7 shows the sorted values against the matrix sparsity s reconstructed at $\sigma = 0.05$. We can clearly see how the calculated T_{ij}^{inf} values closely match the expected blue curve, abruptly falling at the exact matrix sparsity. However, at this stage also the other parameters are active and we are interested in cutting out all those which are irrelevant for the correct description of the \mathbb{T} matrix.

4.1.3 Self-Input coupling

Also Part 3) of \mathbb{M}^{inf} is closely entangled with the noise estimation, cf. Eq. (44). We formally expect $M_{ij} = M_{ji}$, and, as we already said, we implement the symmetry in the minimization procedure. For this part, we compare \mathbb{V}^{inf} with $\mathbb{T}^\dagger \boldsymbol{\beta}^{\text{inf}} \mathbb{T}$, where the \mathbb{T} is the true transmission matrix used to produce the dataset. Part b) of Fig. 7 reveals the appropriateness of the values recovered for the \mathbb{V}^{inf} against the theoretically expected trend, with the inferred set of output channel noises $\boldsymbol{\beta}^{\text{inf}}$.

4.2 Decimation and Information Criterion comparison

The results presented above are referred to the best model learned with all the parameters active in \mathbb{M} . However, this is not always the best choice due to possible overfitting problematics: using all the parameters will fit well the training dataset, but it will poorly perform on the effective estimation of the transmission matrix representing the system, eventually failing the fit procedure on the validation dataset. To avoid this, we are interested in estimating the exact number of parameters active in the channel. We, therefore, proceed as proposed in the decimation procedure, in which we recursively eliminate the smallest couplings, in successive \mathcal{L} -maximization processes. While, doing this, we expect an abrupt change in the \mathcal{L} value at the over- to under-fitting connectivity threshold, which will point out the best model fitting the dataset.

The quality of the inference procedure depends on the sampling rate, Eq. (34), that weights the number of measurements against the number of parameters to be estimated in the model, thus we study the behaviour of our inference method under a variety of numerical conditions. As a function of the linear input size w it is

$$\xi(w) = \frac{M}{K(w)}. \quad (48)$$

By construction the matrix \mathbb{M} has $K(w) = 4w^4$ entries, however taking into account that such matrix is symmetric and that the lower diagonal block in Eq. (5) is diagonal, the number of total independent parameters to be estimated is given by $K(w) = 3/2(w^4 + w^2)$. Furthermore, even though we will always start under the assumption of largest ignorance,

$w \times w$	$\xi(s = 0.2)$	ξ (complete)
4×4	49.21	24.5
8×8	3.37	1.60
12×12	0.68	0.32
16×16	0.22	0.10

Table 1: Sampling ratio for direct (diluted) and inverse (complete) effective transmission matrices for $M = 10000$.

eventually, in the case of the direct transmission matrix inference, this will only have a fraction s of non-zero elements. Therefore the total number of parameters drops to $K = (s + 1/2)w^4 + 3/2w^2$. In the following, considering $M = 10000$ I/O couples, $s = 0.2$ and varying w , we find the sampling ratio values reported in Tab. 4.2 both for the direct (sparse) case and for the inverse (complete) transmission matrix. In both cases the four datasets span a complete sampling scenario, from best to worst.

We, further, run independent optimizations as a function of the noise σ and study the behaviour of the \mathcal{L} progressively eliminating a fraction of $1/128$ couplings at each decimation step. To pick the optimal model among the decimation procedure, we evaluate the information criterions described in Section 3.3, and we compare them on the \mathcal{L} -surface plots in Fig. 9. In each plot, the exact number of parameters to be inferred is represented with a blue line with white dots. Per each sampling rate, we encounter different behaviours, according to the regimes sketched in Sec. 2.3:

- **I/O 4x4** ($\xi \gg 1$): this is the best case for Bayesian inference, all the IC correctly guess the model number at zero noise $\sigma = 0$. As soon as the noise is inserted, the situation changes. AIC and AICc follow the same trend (this is expected since AICc converges to AIC in case of high sampling rate). Both result quite prudent, preferring always models with higher number of parameters. On the other hand, TIC excessively decimates at all the noises. BIC greatly outperforms all the information criteria in this scenario, correctly guessing the parameter number up to $\sigma = 0.36$.
- **I/O 8x8** ($\xi > 1$): the situation changes with respect the previous one. AIC is always very prudent and very stable against noise, while AICc pushes more toward the proper result. However at high noise, AICc excessively decimates. TIC instead, oscillates around the correct value, overdecimating at low noise and underdecimating at higher σ values. BIC correctly guesses the parameter number up to a moderate noise, after that, BIC transits towards excessive decimation. BIC is really not effective for $\sigma \geq 0.16$. Noticeably, at low noise, TIC and BIC closely guess the number of parameters.
- **I/O 12x12** ($\xi \lesssim 1$): the previous behaviour changes in this sampling scenario. AIC is always the most prudent while AICc quickly overdecimates. TIC is very robust at this sampling rate, resulting always very close to the correct solution and never overdecimate. BIC is good up to 10% noise, after that it fails, picking a practically empty model as best guess.
- **I/O 16x16** ($\xi \ll 1$): In this regime, BIC fails at lower noises, recovering exact solutions up to a perturbation of 4%. TIC performs very well, staying prudent at higher noise and

converging to same results as AIC. Remarkably, AICc tends to overfit, favouring results with higher number of active parameters.

We have analyzed how ICs help finding the most accurate number of parameters among the decimated models quantitatively by defining the inference reconstruction error of the \mathbb{T}_{inf} against the original one (used to produce the datasets):

$$Q(\mathbb{T}, \mathbb{T}_{\text{inf}}) = \sqrt{\frac{\|\mathbb{T} - \mathbb{T}_{\text{inf}}\|}{\|\mathbb{T}\|}}. \quad (49)$$

Here, $Q = 0$ corresponds to exact recovery of \mathbb{T}_{inf} and in general low Q represents good inference results. Results are presented in Fig. 10 for all the ICs and model sizes. Remarkably,

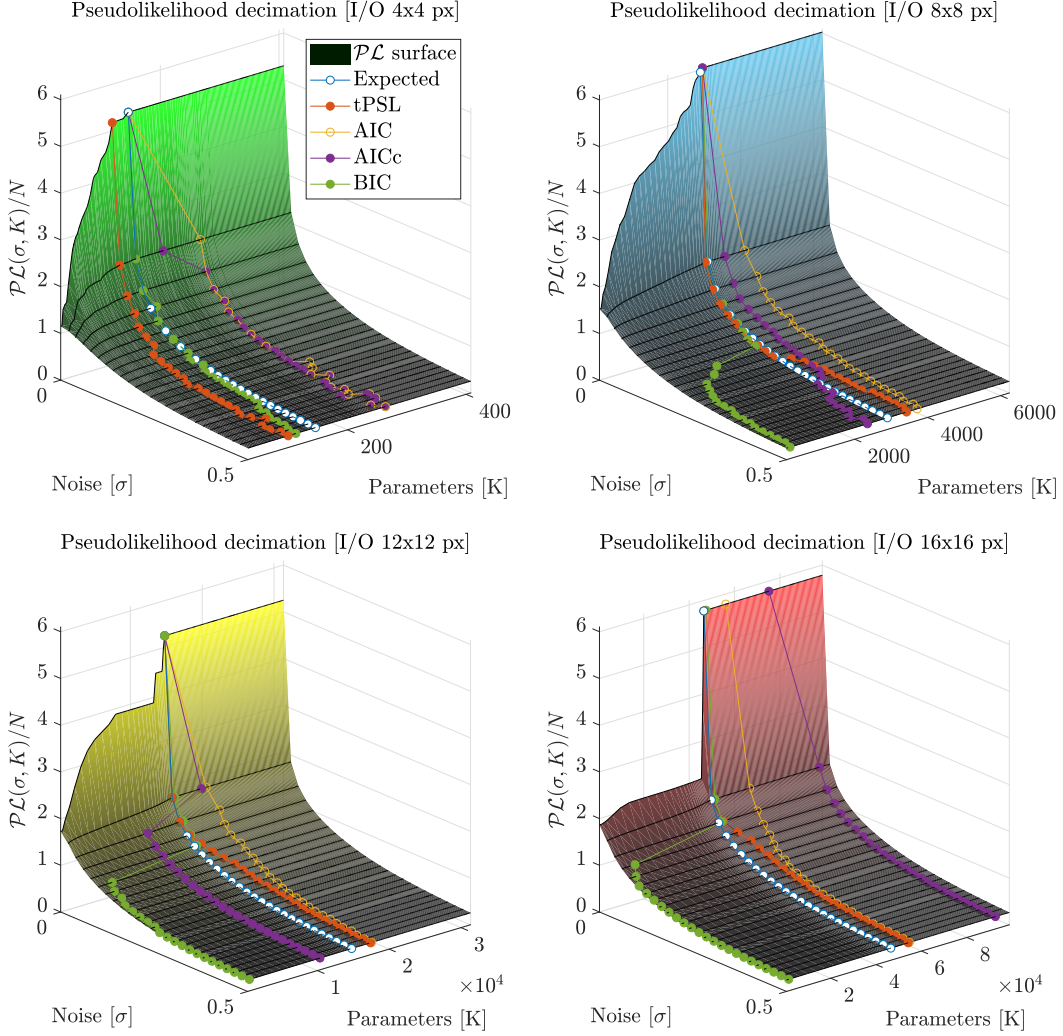


Figure 9: \mathcal{L} -surface plots of four I/O systems tested in this study, differing in the input size w . The surface represent the pseudolikelihood optimized value as a function of the noise and the parameter number (thus, the decimation).

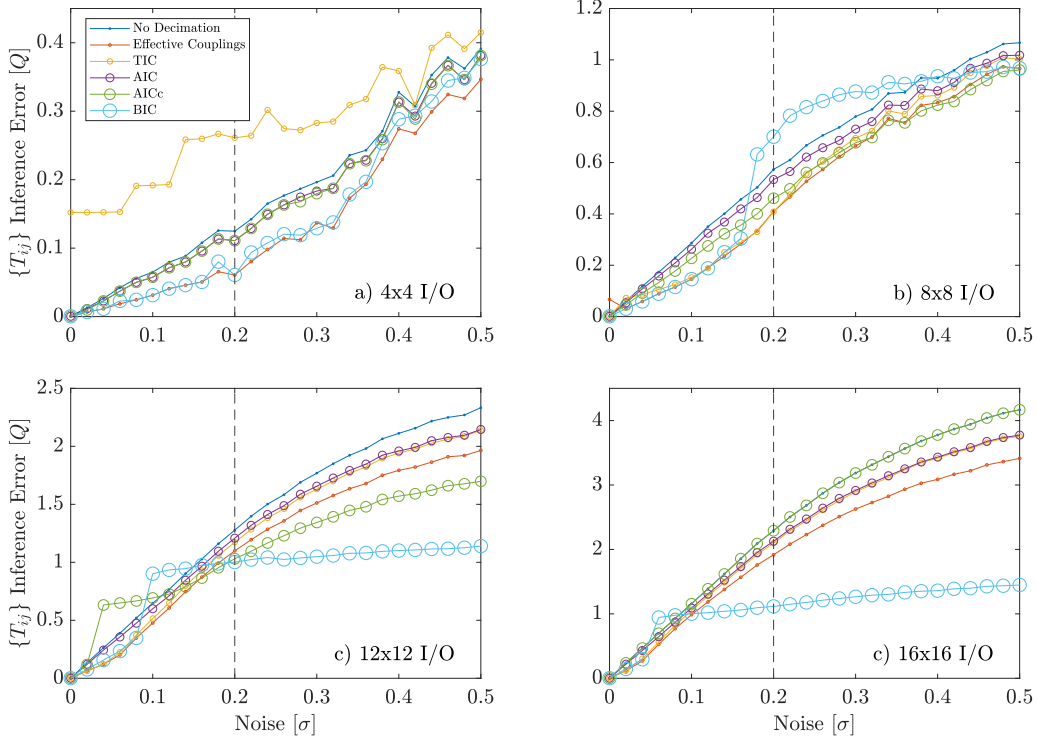


Figure 10: Reconstruction error Q of the direct transmission matrix \mathbb{T}_{inf} . The plots report the quantity Q under different inference scenarios. We can appreciate that all the curves start from $Q \approx 0$, growing as the noise and the size increase (with fixed number of measurements).

at low noise we are able get excellent estimation of \mathbb{T} and at all the sampling rates investigated. Although some IC perform better than others in picking the closest number of parameters, all the models are operatively similar in terms of absolute results. With a few exceptions: TIC poorly performs on oversampled systems (here at 4x4) at any noise and BIC progressively fails at lower noises as ξ decreases. These facts are consistent with the plots of Fig. 9, giving a further indication in favor of an operative equivalence among the different selection criteria tested. In particular, no decimation resulted always worse than the others (thus appropriate decimation worth better results) and knowing the exact number of effective couplings decreases the Q -reference curve.

4.3 The inverse transmission matrix

As already discussed, the same protocol can be used to infer the inverse transmission matrix \mathbb{T}^{-1} , rather than inferring \mathbb{T} and then inverting it. This procedure will be used for the reconstruction of an image pattern that travels from the I-edge to the O-edge, thus to unlock the possibility to use an optically disordered media as a normal objective lens. Let us analyze the reliability on the inference of the inverse, recalling that the dataset was generated with the direct \mathbb{T} matrix. We point out that, in general, the \mathbb{T}^{-1} does not have the same sparsity as the corresponding direct matrix, yet it is a stochastic matrix, as well. We proceed inferring inverse matrices increasing the noise level and the decimation. To be consistent, we present the results in analogy with section 4.2, using the same datasets and colorcode.

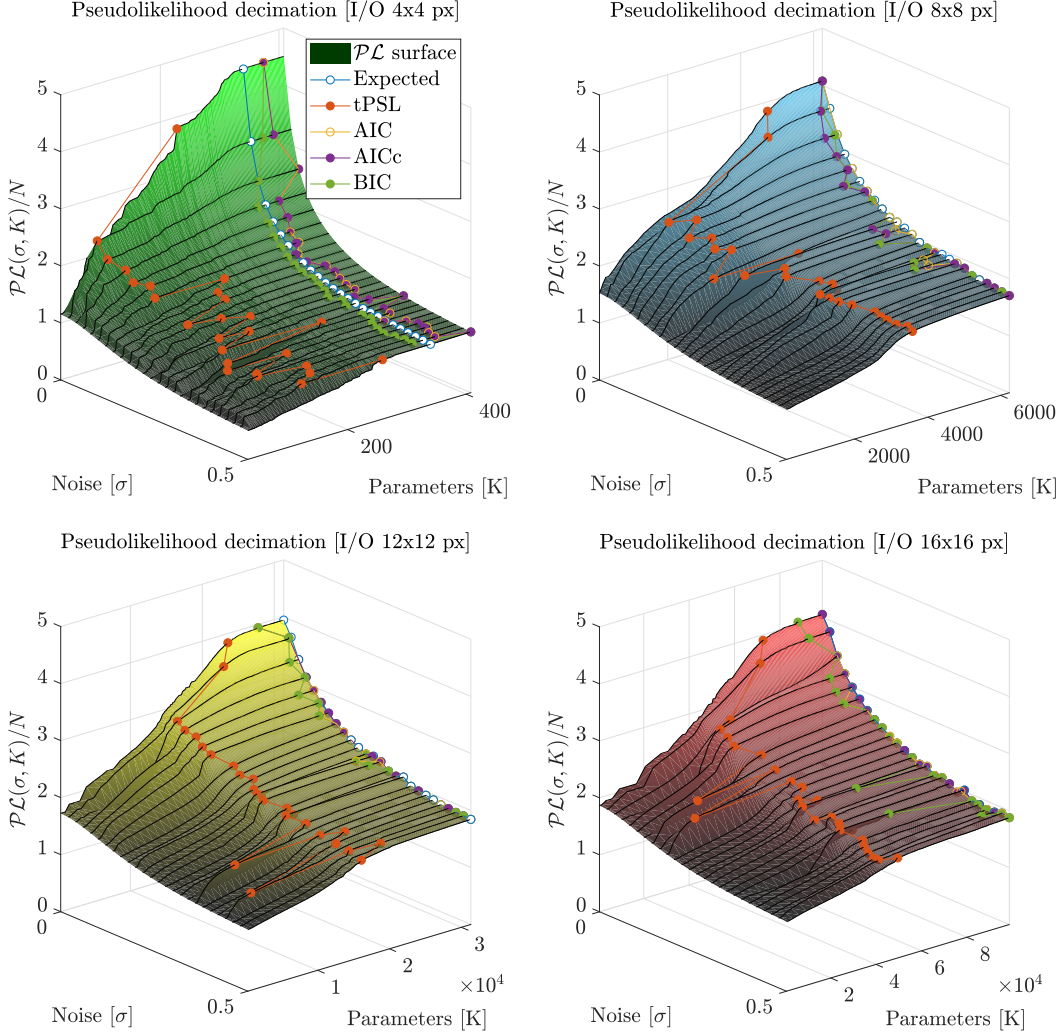


Figure 11: \mathcal{L} -surface plots of several I/O systems tested in this study differing in the input size w . The surface represent the pseudolikelihood optimized value as a function of the noise and the parameter number (thus, the decimation).

- **I/O 4x4** ($\xi \gg 1$): this is the only size at which the inverse matrix has some null entries. Thus, there is a small degree of diluteness to be recovered. In the green \mathcal{L} -surface AIC and AICc are prudent with the decimation, BIC gets closer to the actual value of parameters to be estimated slightly preferring setting to zero smaller couplings. Interestingly, TIC strongly decimates and has a less predictable behaviour, with strong fluctuation at high noise.
- **I/O 8x8** ($\xi \gtrsim 1$): at this size the \mathbb{T}^{-1} is not sparse at all and, accordingly, AIC, AICc and BIC always determine a weak or no decimation. Like in the previous case, TIC tends to overdecimate the coupling matrix.
- **I/O 12x12** ($\xi < 1$): In this case, the situation is pretty similar to the 8x8 case, being TIC the worse information criterion among the others.

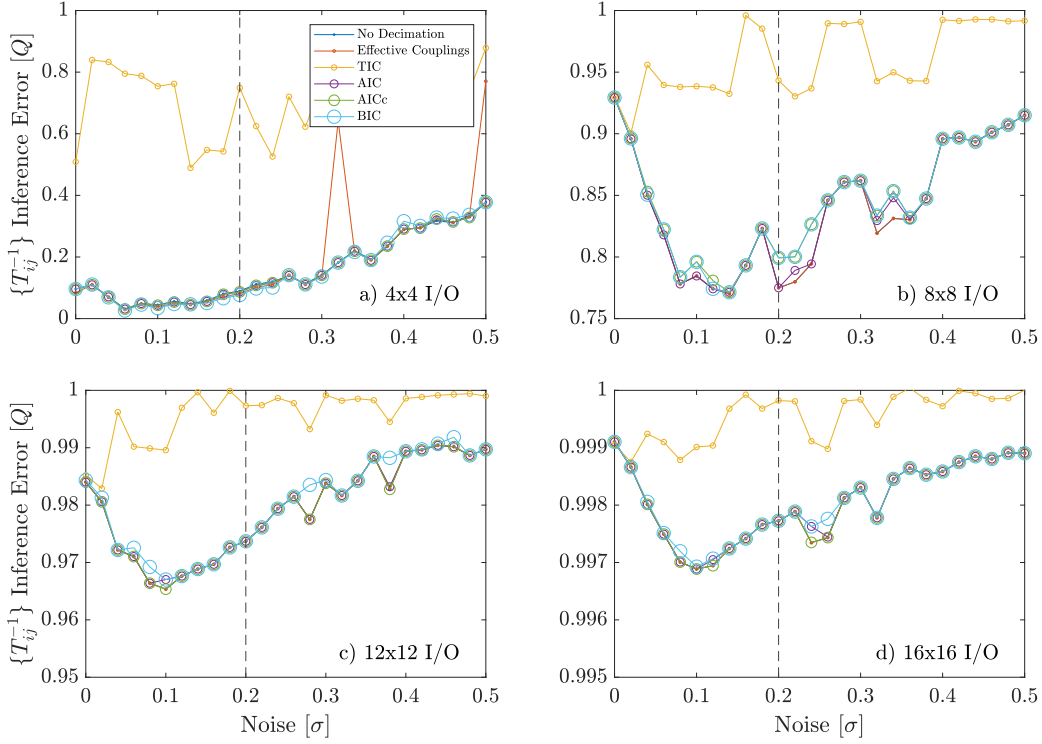


Figure 12: Reconstruction error of the inverse transmission matrix $\mathbb{T}_{\text{inf}}^{-1}$. We plot the quantity Q under different inference scenarios. Contrarily to Fig. 10, the curves do not start from zero, even if for the smallest system the error is quite low and grows with the noise. In all the other cases, the error is always quite high, having a minimum around $\sigma = 0.1$.

- **I/O 16x16** ($\xi \ll 1$): With the biggest system considered BIC tends to excessively decimate compared with AIC and AICc, which are the most accurate selection criteria. TIC fails like the previous cases, returning always a quite sparse matrix.

Interestingly, for the \mathbb{T}^{-1} inference TIC always produced wrong estimation, strongly decimating coupling while the matrix was not sparse. This is more a test on TIC (and other IC, in general), then on the inference quality itself. Indeed, being \mathbb{T}^{-1} a dense matrix we know in advance that any decimation trial should be irrelevant. In principle, no elements are zero, though many can be small, because of the stochasticity property $\sum_j T_{ij}^{-1} = 1$ (we recall that \mathbb{T} is a stochastic matrix, with random entries $T_{ij} \in [0, 1]$ and $\sum_j T_{ij} = 1$). So decimating setting the smallest ones to zero, or leaving them undecimated, does not, actually, change the reconstruction outcome.

Yet, we have to take into account several issues, some strictly numerical. In a certain sense, the matrix \mathbb{T}^{-1} was not directly controlled nor normalized (in the direct case we had full control on the definition of \mathbb{T}), and to estimate it we have to rely on numerical inversion techniques. Moreover, \mathbb{T}^{-1} has also access to negative values that vary along each line, and the condition $\sum_j T_{ij}^{-1} = 1$ is not constraining the magnitude of the entries that can become large if proper cancellations occur. In these terms, the inference of direct- and inverse- \mathbb{T} represent two opposite scenarios.

To control the inference quality in the inverse regime, we compute the reconstruction

error $Q\left(\mathbb{T}^{-1}, (\mathbb{T}^{-1})_{\text{inf}}\right)$ like in section 4.2. Compared to the situation described previously, we never reach $Q \approx 0$ in any reconstruction. Moreover, seems that there is an optimal noise around $\sigma \approx 0.1$ at which the inference is slightly more accurate (minimum in the Q curve). Again, all the IC selections tightly follow the same quality-trend being almost indistinguishable, with TIC quickly departing from good estimations already at $\sigma = 0.04$. By looking at both Fig. 11 and 12, it seems clear that TIC is not reliable while inferring \mathbb{T}^{-1} . TIC in fact, grounds its estimation based on sensitive features of the pseudo-likelihood curve: a net drop of the \mathcal{L} is picked easily with TIC, while noisy curves could missplace its maximum. Moreover, by its definition, the TIC cannot be used if the matrix is densely populated. TIC is defined to be zero at full or empty matrix connectivity, thus its maxima cannot be located at its edges.

4.4 Pseudo-unity product

Consistency is important especially when evaluating both \mathbb{T} and its inverse independently. Thus, it is worth to study the product $\mathbb{T}^{-1}\mathbb{T} = \mathbb{T}\mathbb{T}^{-1} = \mathbb{I}$. The inference procedures are performed separately for each of the two matrices, consequently we are not guaranteed that this property is preserved during the inference. Moreover, we used different IC selections, that might perform better on direct or inverse inference but not with both, since \mathbb{T} is sparse but \mathbb{T}^{-1} is dense. We tested the consistency of the method picking the best inferred matrices (direct and inverse) and multiplying each other, in order to estimate the identity matrix. Per each w we use the information criterion that best matched the right number of couplings of the direct matrix, without any consideration for the inverse. In the plot of Fig. 13 we plot the sorted values of the pseudo-unity matrix $(\mathbb{T}^{-1})_{\text{inf}} \mathbb{T}_{\text{inf}}$ calculated in the $w = 4$ case, choosing AIC as the best selection criterion for both direct and inverse.

We use a progressive colormap to differentiate between reconstructions at different noise. In low noise transmission (bluish curves), the diagonal strongly dominates over the out-of-diagonal region, exhibiting a visible step that tends to vanish as the rumour increases. However, we found that a dominant diagonal feature emerged at all the noises considered. For all the other size explored we found similar behaviour, with the general trend that the higher the number of measurements M the better is the reconstruction of the diagonal part of the pseudo-unity matrix. As already discussed in section 4.3, TIC cannot be used to pick inverse matrices due to the fact that it is not devised for dense matrices.

4.5 Testing image transmission and focusing

The ultimate goal of this study, is to create a statistical framework able to recover the transmission matrix of a optical disordered system via a random sampling approach, opening the possibility to use turbid media as optically opaque lenses. Ideally, one wants a reliable system, able to correctly infer the properties of the channel on both directions even in the presence of strong noise fluctuation and saturation effects. To test the robustness of the inference procedure, we decided to accomplish two tasks defined in this way:

- **Focusing:** using the inferred \mathbb{T}_{inf} matrix to deliver energy to a given spatial pattern at the output. From the knowledge of \mathbb{T}_{inf} we are able to construct a given output pattern (like focusing on a given spot) changing the input.

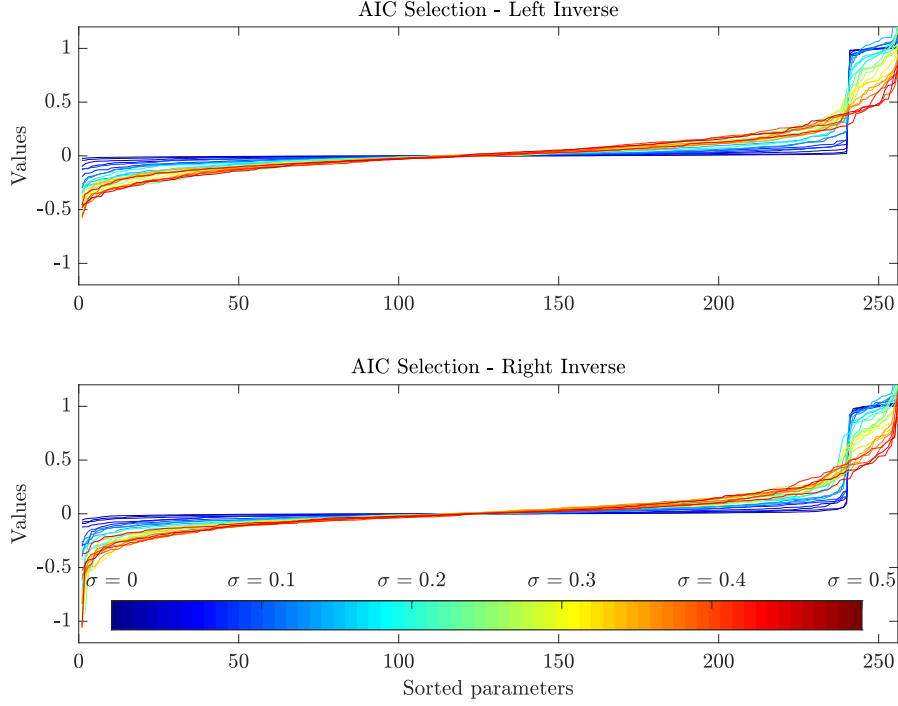


Figure 13: Sorted values of the matrix $(\mathbb{T}^{-1})_{\text{inf}} \mathbb{T}_{\text{inf}}$ (top) and $\mathbb{T}_{\text{inf}} (\mathbb{T}^{-1})_{\text{inf}}$ (bottom) obtained with AIC selection with a 4x4 system. The baseline of the identity matrix is drawn with a black solid line, while the sorted values at increasing noise are plotted following a progressive colorcode. The bluish lines (low σ) are closely following the expected behaviour, having a strong diagonal component dominating a almost null out of diagonal region. The situation progressively worsens at increased noise, though diagonal elements remain larger than the off-diagonal ones.

- **Imaging:** using the inferred $(\mathbb{T}^{-1})_{\text{inf}}$ matrix to reconstruct the image of an object at the input starting from the noisy and random pattern in output.

In a perfect scenario, it might be reasonable to believe that both situations are equivalent reversing the input-output order in the vector containing the pixel intensities \mathbf{I} , due to the exchange of role between \mathbb{T} and \mathbb{T}^{-1} .

To test the inferred matrices we take a further validation dataset \mathbf{I}_{val} composed of $M' = 1000$ new patterns that we transmit through the disordered channel. This important test acts as a validation for the training procedure, given that none of these \mathbf{I}_{val} vectors were used in the learning dataset. By using \mathbb{T}_{inf} and $\left[(\mathbb{T}^{-1})_{\text{inf}}\right]^{-1}$ we want to reconstruct the intensity pattern focused at the output, $\mathbf{I}_{\text{rec}}^{\text{out}}$, given an input. On the other hand by using $(\mathbb{T}^{-1})_{\text{inf}}$ and $(\mathbb{T}_{\text{inf}})^{-1}$ we want to reconstruct the image at the input, $\mathbf{I}_{\text{rec}}^{\text{in}}$, given a pattern at the output. To test the goodness of the reconstructions, we calculate the connected correlation C between

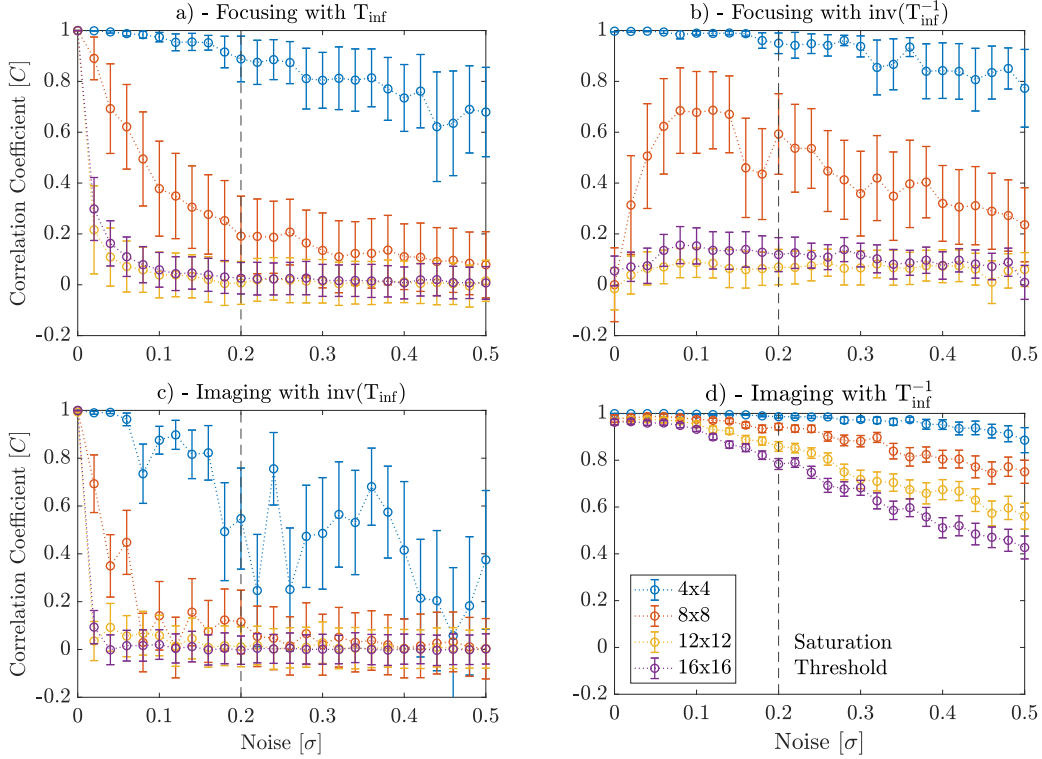


Figure 14: Correlation of the reconstructed patterns using the inferred \mathbb{T} and \mathbb{T}^{-1} and their corresponding inverted quantities.

the true \mathbf{I}^x and the reconstructed object $\mathbf{I}_{\text{rec}}^x$, being $x = \text{in, out}$:

$$C(\mathbf{I}^x, \mathbf{I}_{\text{rec}}^x) = \frac{\sum_l (\mathbf{I}^x - \bar{\mathbf{I}}^x) (\mathbf{I}_{\text{rec}}^x - \bar{\mathbf{I}}_{\text{rec}}^x)}{\sqrt{\left[\sum_l (\mathbf{I}^x - \bar{\mathbf{I}}^x)^2 \right] \left[\sum_l (\mathbf{I}_{\text{rec}}^x - \bar{\mathbf{I}}_{\text{rec}}^x)^2 \right]}} \quad (50)$$

where $l = \{\alpha, \gamma\}$ and $\bar{\mathbf{I}}^x$ is the mean value of \mathbf{I}^x . $C = 1$ means exact reconstruction whereas a small C means failed reconstruction. In principle C could also access negative values, being $C = -1$ a perfectly reconstructed object with opposite sign.

We report the analysis of the correlation behavior for focusing and for imaging versus sampling rate and noise in Fig. 14, where the transmission matrices used were inferred by pseudo-likelihood-maximization and AIC decimation.

Focusing

- Focusing with \mathbb{T}_{inf} : it works extremely well at zero noise for any system linear size w . The correlation drops as soon as we increase the noise, decreasing the faster, the smaller the sampling rate. For $\xi < 1$ the focusing is substantially lost as soon as $\sigma > 0$, whereas for $\xi \gg 1$ the focusing with the real and the inferred matrices yield very correlated results also with a large noise $\sigma = 0.5$.
- Focusing with $\left[(\mathbb{T}^{-1})_{\text{inf}} \right]^{-1}$: the inversion of the $\mathbb{T}_{\text{inf}}^{-1}$ appears to be robust against inversion at high sampling rate for any noise, quickly dropping as $\xi \geq 1$. In these cases

the correlation behavior is not monotonous with the noise but there seems to be an optimal noise value ($\sigma \approx 0.1$) at which the inversion returns the best result.

Imaging

- c) Imaging with $(\mathbb{T}_{\text{inf}})^{-1}$: one of the main point of our study lies here. In fact, the numerical inversion of \mathbb{T}_{inf} is highly unstable already at moderate noise for practically any sampling rate ξ . At $\sigma = 0$, however, numerical inversion was correctly outperformed at all investigated sizes, even for $\xi \ll 1$.
- d) Imaging with $(\mathbb{T}^{-1})_{\text{inf}}$: quite impressive results are found for the inverse inference. The correlation with the true pattern remains quite stable in the whole noise range explored, moreover being robust at any sampling scenario.

At this point of our study the situation is quite clear, matrix inversion is something that we need to avoid, especially in the presence of the noise. Both the matrix inversions resulted into less (or not-at-all) robust reconstruction, thus is always better to directly infer the matrix needed for the given application: focusing or imaging . At the simple cost of doubling the inference time we have access to full characterization of the disordered system, more robust against noise. The problem still scales linearly with the size of the system and it is still possible to perform independent parallelization.

5 Conclusions and Perspectives

At the end of such a long journey, we want to briefly discuss and recap some important aspects emerged from our study. First of all, our study wants to point out that relying to matrix inversion after the inference of \mathbb{T} is a practice that is better to avoid in presence of non-negligible noise and small data sets (or large number of parameters to learn). Our model is equivalently reversible and accepts I/O swap, giving access to direct inference of the \mathbb{T}^{-1} . As a last additional analysis, let us examine the correlation coefficient of the $C(\mathbb{T}, \mathbb{T}_{\text{inf}})$ and $C(\mathbb{T}^{-1}, \mathbb{T}_{\text{inf}}^{-1})$. The results are presented in Fig. 15 as a function of the noise and the IC used for selecting among decimated models.

In panel a) the results of the correlation of the inferred transmission matrix against the true matrix are intuitive. The green curves prove better results when sampling $\xi \gg 1$, returning excellent correlation in the whole noise range explored. The situation progressively worsens as soon as ξ decreases below 1, i. e., the number of parameter becomes larger than the measurements used for the learning. On the other hand, we could look at the correlation trend of the $\mathbb{T}_{\text{inf}}^{-1}$, reported in part b). It is standing out a pretty different situation. Only the $\xi \gg 1$ case behaved like in the previous inference, where the others start from lower correlation at low noise. Afterwards, the correlation reaches a maximum then decreases again. The same behavior can be observed for any size, though for the two larger sizes of 12x12 and 16x16, the correlation with the original inverse matrix is so low that we may suspect poor reconstruction performances.

Since the \mathbb{T} , and consequently \mathbb{T}^{-1} , is stochastic, it is interesting to observe if this property is recovered by the inference process, in which stochasticity is not imposed. Per each AIC reconstruction, we calculate the average row sum of \mathbb{T}_{inf} and $(\mathbb{T}_{\text{inf}})^{-1}$ that we plot against

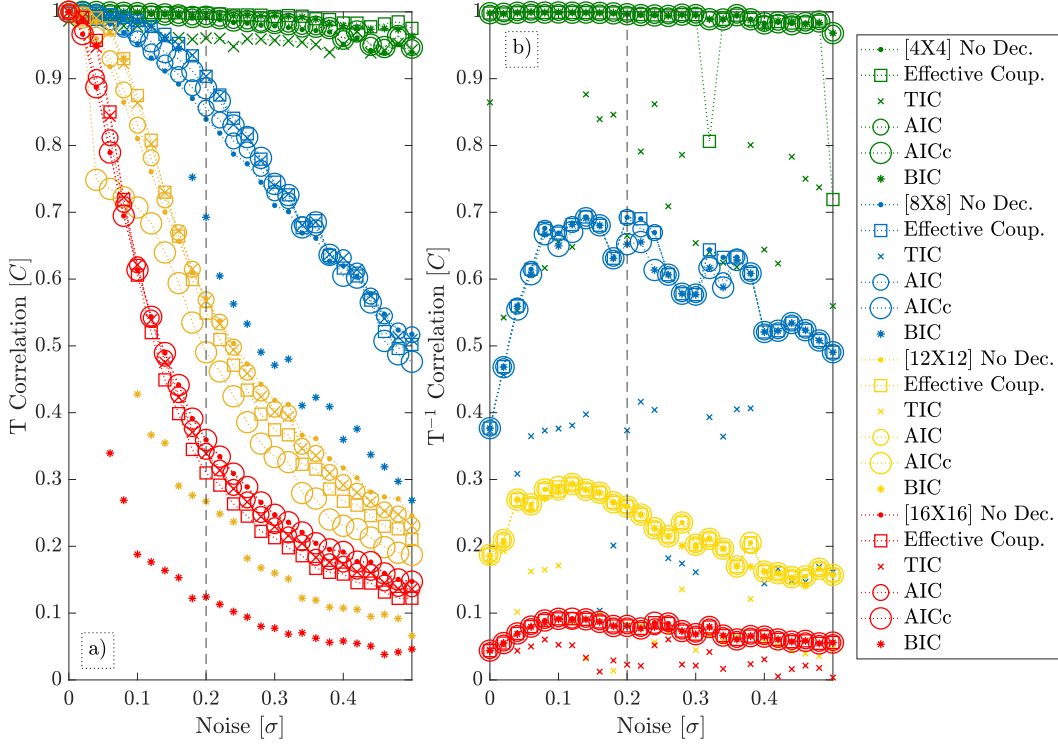


Figure 15: Part a), correlation of the \mathbb{T}_{inf} with the original one used to create both training and validation dataset as a function of the noise and for the various IC used. We can notice how every curve start with $C \approx 1$ decaying faster as the system size increases. Part b), $\mathbb{T}_{\text{inf}}^{-1}$ correlation against the expected one. Here we notice a particularly low correlation, especially in the bigger (and undersampled) systems.

the noise in Fig. 16. It is visible that the matrices recovered at any size and at low noises are stochastic. However, above the saturation threshold, the stochasticity starts to have strong fluctuations and its mean value decreases considerably. It is remarkable that the trend followed at every system size seems to coincide regardless of the sampling ratio.

The correlation plot of Fig. 15 seems to condemn the inference of \mathbb{T}^{-1} to low quality reconstructions in the case of low sampling rate. On the contrary, though, we tested such matrices obtaining very robust reconstructions for the validation set in Fig. 14. Let us, then, have a look at an image reconstructed using $(\mathbb{T}^{-1})_{\text{inf}}$ and using $(\mathbb{T}_{\text{inf}})^{-1}$ (also termed $\text{inv}(\mathbb{T}_{\text{inf}})$ in the figures). As a test image we use a 16x16 image of a little bomb, reconstructing the image propagating from the output back to the input edge. The reconstructions are presented in Fig. 17 using $(\mathbb{T}_{\text{inf}})^{-1}$ (set on top) and $(\mathbb{T}^{-1})_{\text{inf}}$ (bottom). In the first case, the reconstruction is perfect at zero noise, but its quality immediately drops and the image is not recognizable at any noise other than $\sigma = 0$. The latter, instead, returns remarkable reconstructions at finite noise, even if the \mathbb{T}^{-1} -correlation plot was poor and the reconstruction error Q was large. At noises around the saturation threshold $\sigma \neq 0.2$ the reconstructions start to fade into noisy background.

At this point, we can sum up our take home message: the inversion process carried on a matrix inferred by pseudo-likelihood maximization on undersampled training dataset leads

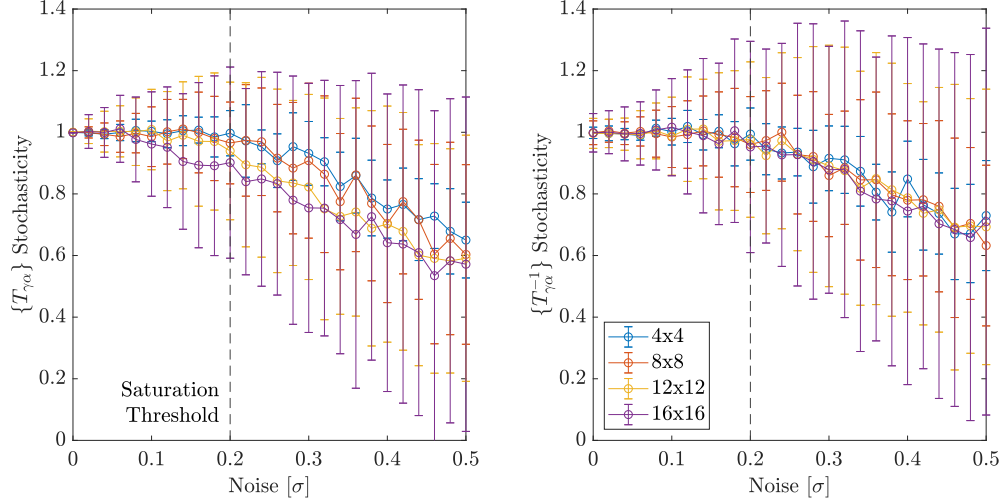


Figure 16: Measure of the stochasticity of the inferred matrix. We can notice that at zero noise is fully recovered in both cases, while increasing the noise the stochasticity decreases with huge fluctuations along lines.

to poor results, as expected. In our framework, though, the inference of the inverse seems performing well even when datasets are small and offers an extra tool exploitable for focusing or imaging through disordered channels. The inference procedure on the inverse transmission matrix for low sampling ratio's yields a matrix that does not reproduce well the original one, yet (i) gives the identity matrix when multiplied to the direct \mathbb{T} and (ii) performs high quality image reconstruction when used on validation data sets.

Although the model Eq. (1) is not rigorously correct for coherent field summation, it is a first approximation necessary to deal with intensity only data and a first step to consider the inaccessibility of mode phases. This article, in fact, has to be considered as a complete treatise on the method firstly introduced in [32]. The vastness of the results found pushed us toward a full characterization of the learning framework introduced. As work in progress we are developing an algorithm that takes into account the impossibility to access to phase measurements both at input and output edges [23]. Our approach is to calculate the \mathcal{L} performing first a weighted integral over the unknown phases with a Boltzmann equilibrium measure, i. e., under the same hypothesis of Eq. (6). In this way, we obtain an expression of \mathcal{L} usable for intensity measurements in which, at the same time, the parameters to be inferred are the elements of the actual transmission matrix (i. e., part of the scattering matrix) of the object crossed by the light, and not an effective matrix connecting I/O pixels. Therefore, this will also allow to study properties of the structure of the materials composing the medium, on top of yielding a tool for focusing and/or image reconstruction.

Among conventional focusing and imaging through disordered media [7, 33], our approach finds a major application for the comprehension of structured focusing [34, 35], to study Anderson localization in disordered fibers [36] or signal transmission through hyperuniform channels [37]. Moreover, the bidirectional approach let our framework consistent for the study of truncated channels: when observing a fiber, we can look at the whole fiber's output compared with the whole input, while this is not always true in case the observation is done in a confined output region [33]. Leaving open channels in the system leads the impossibility

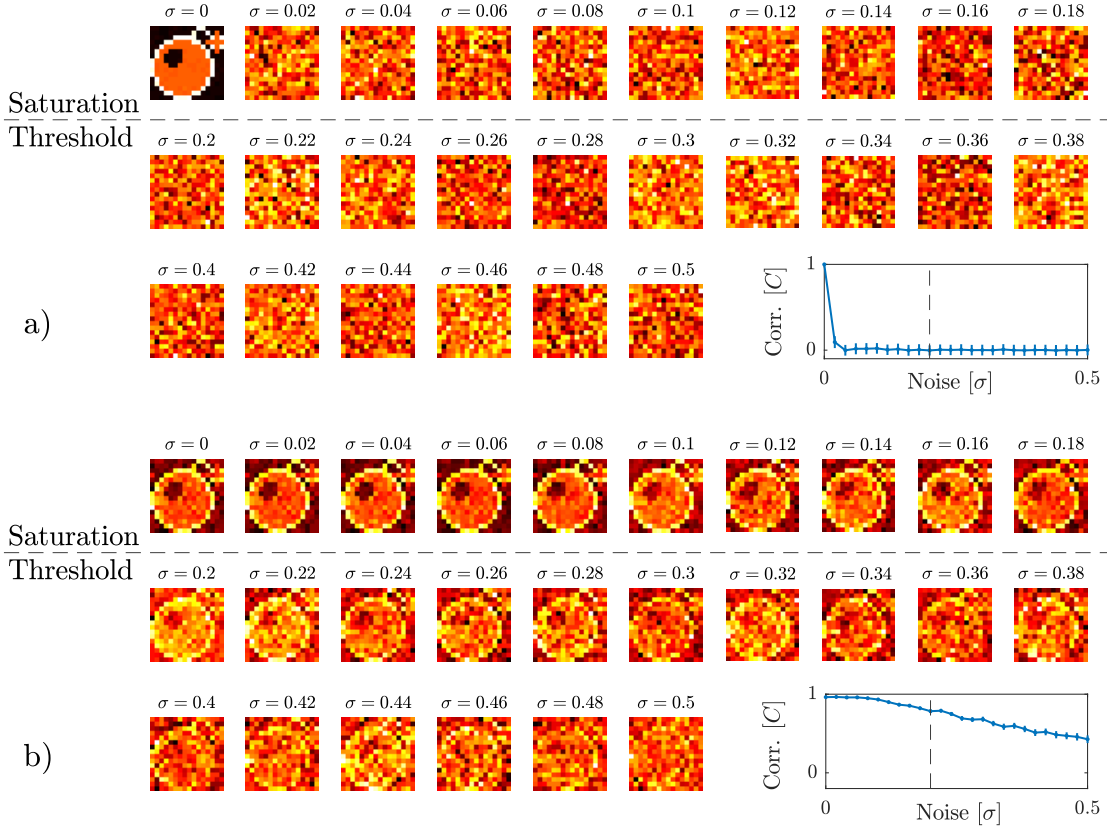


Figure 17: Upper part a), image reconstructions using $(\mathbb{T}_{\text{inf}})^{-1}$ and bottom part b), using $(\mathbb{T}^{-1})_{\text{inf}}$. The insets reproduce the correlation between the image reconstructed with the original and with the inferred transmission matrices, cf. the 16×16 curves of panel c) (top) and d) (bottom) of Fig. 14. It is possible to notice how the performance are better in the inverse inference at any noise, where the direct gives excellent reconstruction only at zero noise.

of \mathbb{T} -matrix inversion, and forces us to infer directly its inverse.

Even though we used as example the case of the transmission matrix recovery in a disordered optical tool, our results are generally extendible for any linear system solution and has a broad application spectrum, especially in the context of supervised machine learning [1, 2]. A particular feature of our model is that a lot of information is encoded in the interaction matrix \mathbb{M} other than the transmission matrix alone. In fact, we are automatically obtaining an estimation of the noise variance under Gaussian statistics (thus giving estimation on the presence of more noisy channels) and the self-input coupling term is proportional to the Gramian matrix that can be exploited for further analysis [38].

From a technical point of view, one important feature is the linear scalability in the model complexity as function of the dimension of the system considered. Each partial likelihood term \mathcal{L}_i is an independent entity and their summation can always be parallelized among the hardware resources. Our model, in fact, finely fits the GPU requirements and it is directly parallelizable in CUDA. Last, but not least, this work was inspired by recent development

in statistical mechanics of random optical systems [39–41], either from thermodynamics and from inference work [25, 26]. From this world we borrowed a number of ideas [19, 25] and further tools could be linked to expand the results to further cases, studying for example phase transitions between feasible and unfeasible inference scenarios.

Acknowledgements

The authors thank A. Marruzzo, G. Gradenigo, F. Antenucci, J. Rocchi, F. Ricci-Tersenghi, L. Biferale, for useful discussions.

Funding information The research leading to these results has received funding from the Italian Ministry of Education, University and Research under the PRIN2015 program, grant code 2015K7KK8L-005 and the European Research Council (ERC) under the European Union’s Horizon 2020 research and innovation program, project LoTGlasSy, Grant Agreement No. 694925.

References

- [1] C. Robert, *Machine learning, a probabilistic perspective* (2014).
- [2] J. Friedman, T. Hastie and R. Tibshirani, *The elements of statistical learning*, vol. 1, Springer series in statistics New York, NY, USA: (2001).
- [3] R. Peckner, S. A. Myers, A. S. V. Jacome, J. D. Egertson, J. G. Abelin, M. J. MacCoss, S. A. Carr and J. D. Jaffe, *Specter: linear deconvolution for targeted analysis of data-independent acquisition mass spectrometry proteomics*, *Nature methods* **15**(5), 371 (2018).
- [4] E. Altay and M. H. Satman, *Stock market forecasting: artificial neural network and linear regression comparison in an emerging market*, *Journal of Financial Management & Analysis* **18**(2), 18 (2005).
- [5] S. M. Popoff, G. Lerosey, M. Fink, A. C. Boccara and S. Gigan, *Controlling light through optical disordered media: Transmission matrix approach*, *New Journal of Physics* **13**(12), 123021 (2011), doi:10.1088/1367-2630/13/12/123021, 1107.5285.
- [6] J. Bertolotti, E. G. van Putten, C. Blum, A. Lagendijk, W. L. Vos and A. P. Mosk, *Non-invasive imaging through opaque scattering layers*, *Nature* **491**(7423), 232 (2012).
- [7] I. M. Vellekoop, A. Lagendijk and A. P. Mosk, *Exploiting disorder for perfect focusing*, *Nature photonics* **4**(5), 320 (2010).
- [8] P. Sebbah, *Waves and imaging through complex media*, Springer Science & Business Media (2001).
- [9] J. Yoon, K. Lee, J. Park and Y. Park, *Measuring optical transmission matrices by wavefront shaping*, *Optics Express* **23**(8), 10158 (2015).

- [10] J. Carpenter, B. J. Eggleton and J. Schröder, *110x110 optical mode transfer matrix inversion*, Optics Express **22**(1), 96 (2014), doi:10.1364/OE.22.000096.
- [11] D. S. Wiersma, *Disordered photonics*, Nature Photonics **7**(3), 188 (2013).
- [12] D. E. Boonzajer Flaes, J. Stopka, S. Turtaev, J. F. De Boer, T. Tyc and T. Čižmár, *Robustness of Light-Transport Processes to Bending Deformations in Graded-Index Multimode Waveguides*, Physical Review Letters **120** (2018), doi:10.1103/PhysRevLett.120.233901.
- [13] T. Chaigne, O. Katz, A. C. Boccara, M. Fink, E. Bossy and S. Gigan, *Controlling light in scattering media non-invasively using the photoacoustic transmission matrix*, Nature Photonics **8**(1), 58 (2014).
- [14] H. Frostig, E. Small, A. Daniel, P. Oulevey, S. Derevyanko and Y. Silberberg, *Focusing light by wavefront shaping through disorder and nonlinearity*, Optica **4**(9), 1073 (2017), doi:10.1364/OPTICA.4.001073.
- [15] R. Penrose, *On best approximate solutions of linear matrix equations*, In *Mathematical Proceedings of the Cambridge Philosophical Society*, vol. 52, pp. 17–19. Cambridge University Press (1956).
- [16] P. Tyagi, A. Marruzzo, A. Pagnani, F. Antenucci and L. Leuzzi, *Regularization and decimation pseudolikelihood approaches to statistical inference in xy spin models*, Phys. Rev. B **94**, 24203 (2016).
- [17] P. Ravikumar, M. J. Wainwright and J. D. Lafferty, *High-dimensional ising model selection using ℓ_1 regularized logistic regression*, Ann. Statist. **38**, 1287 (2010).
- [18] M. Ekeberg, C. Lövkvist, Y. Lan, M. Weigt and E. Aurell, *Improved contact prediction in proteins: Using pseudolikelihoods to infer potts models*, Phys. Rev. E **87**, 012707 (2013), doi:10.1103/PhysRevE.87.012707.
- [19] A. Decelle and F. Ricci-Tersenghi, *Pseudolikelihood decimation algorithm improving the inference of the interaction network in a general class of ising models*, Physical Review Letters **112**(7) (2014), doi:10.1103/PhysRevLett.112.070603, arXiv:1304.0942v4.
- [20] D. Kim, J. Moon, M. Kim, T. D. Yang, J. Kim, E. Chung and W. Choi, *Toward a miniature endomicroscope: pixelation-free and diffraction-limited imaging through a fiber bundle*, Optics letters **39**(7), 1921 (2014).
- [21] S. M. Popoff, G. Lerosey, M. Fink, A. C. Boccara and S. Gigan, *Controlling light through optical disordered media: transmission matrix approach*, New. J. Phys. **13**, 123021 (2011).
- [22] R. D. L. S. Bianchi, *A multi-mode fiber probe for holographic micromanipulation and microscopy*, Lab Chip **12**, 635 (2012).
- [23] D. Ancora, R. Verratti and L. Leuzzi, *How to deal with the lack of mode phase measurements in transmission matrix reconstruction for imaging and focusing*, in preparation (2019).
- [24] D. Barber, *Bayesian reasoning and machine learning*, Cambridge University Press (2012).

- [25] P. Tyagi, A. Marruzzo, A. Pagnani, F. Antenucci and L. Leuzzi, *Regularization and decimation pseudolikelihood approaches to statistical inference in XY spin models*, Physical Review B **94**(2), 24203 (2016), doi:10.1103/PhysRevB.94.024203, 1603.05101.
- [26] A. Marruzzo, P. Tyagi, F. Antenucci, A. Pagnani and L. Leuzzi, *Improved Pseudolikelihood Regularization and Decimation methods on Non-linearly Interacting Systems with Continuous Variables*, SciPost Phys **5**, 2 (2017), doi:10.21468/SciPostPhys.5.1.002, 1708.00787.
- [27] M. Schmidt, *minfunc: unconstrained differentiable multivariate optimization in matlab*, Software available at <http://www.cs.ubc.ca/~schmidtm/Software/minFunc.htm> (2005).
- [28] H. Akaike, *A new look at the statistical model identification*, IEEE transactions on automatic control **19**(6), 716 (1974).
- [29] C. M. Hurvich and C.-L. Tsai, *Regression and time series model selection in small samples*, Biometrika **76**(2), 297 (1989).
- [30] G. Schwarz *et al.*, *Estimating the dimension of a model*, The annals of statistics **6**(2), 461 (1978).
- [31] S. Franz, F. Ricci-Tersenghi and J. Rocchi, *A fast and accurate algorithm for inferring sparse ising models via parameters activation to maximize the pseudo-likelihood*, arXiv preprint arXiv:1901.11325 (2019).
- [32] D. Ancora and L. Leuzzi, *Learning direct and inverse transmission matrices*, arXiv preprint (2019), arXiv:1901.04816.
- [33] S. Popoff, G. Lerosey, M. Fink, A. C. Boccarda and S. Gigan, *Image transmission through an opaque material*, Nature Communications **1**(6) (2010), doi:10.1038/ncomms1078, 1005.0532.
- [34] D. Di Battista, D. Ancora, M. Leonetti and G. Zacharakis, *Tailoring non-diffractive beams from amorphous light speckles*, Applied Physics Letters **109**(12), 121110 (2016), doi:10.1063/1.4962955.
- [35] D. Di Battista, D. Ancora, H. Zhang, K. Lemonaki, E. Marakis, E. Liapis, S. Tzortzakos and G. Zacharakis, *Tailored light sheets through opaque cylindrical lenses*, Optica **3**(11), 1237 (2016).
- [36] M. Leonetti, S. Karbasi, A. Mafi and C. Conti, *Observation of migrating transverse anderson localizations of light in nonlocal media*, Physical Review Letters **112**(19) (2014), doi:10.1103/PhysRevLett.112.193902, arXiv:1407.7990v1.
- [37] D. Di Battista, D. Ancora, G. Zacharakis, G. Ruocco and M. Leonetti, *Hyperuniformity in amorphous speckle patterns*, Optics Express **26**(12), 15594 (2018).
- [38] V. Sreeram and P. Agathoklis, *On the properties of gram matrix*, IEEE Transactions on Circuits and Systems I: Fundamental Theory and Applications **41**(3), 234 (1994).

- [39] F. Antenucci, A. Crisanti and L. Leuzzi, *Complex spherical $2+4$ spin glass: A model for nonlinear optics in random media*, Phys. Rev. A **91**, 053816 (2015).
- [40] F. Antenucci, A. Crisanti, M. Ibañez Berganza, A. Marruzzo and L. Leuzzi, *Statistical mechanics models for multimode lasers and random lasers*, Phil. Mag. **96**, 704 (2016).
- [41] F. Antenucci, *Statistical physics of wave interactions*, Springer (2016).